

Department of Physics and Astronomy

University of Heidelberg

Master thesis

in Physics

submitted by

Maximilian Prüfer

born in Wiesbaden

2016

**Structure Formation in a Quenched
Antiferromagnetic Spinor Bose-Einstein Condensate**

This Master thesis has been carried out by Maximilian Prüfer

at the

Kirchhoff-Institute for Physics

under the supervision of

Prof. Dr. Markus K. Oberthaler

Structure Formation in a Quenched Antiferromagnetic Spinor Bose-Einstein Condensate

In this thesis, we study the structure formation following a quench of the detuning of spin exchange. For this, we employ an effective spin-1 ^{87}Rb Bose-Einstein condensate in a one-dimensional situation. Bogoliubov theory predicts unstable momentum modes for specific regimes of the detuning. These are populated by spin-changing collisions and the emerging structure can be observed in the transversal spin directions.

We present our experimental system and discuss the relevant parameters. After introducing two analysis methods, the spin Fourier spectrum and the spatial correlation function, we compare the homogeneous Bogoliubov theory to the experimentally obtained results for short evolution times. The characteristic structure size follows the theoretical predictions. Further, we discuss longer evolution times where the Bogoliubov approximation becomes invalid. The observed behaviour can be partially understood by an altered interaction strength due to the depletion of the condensed mode. We see first indications for emerging structures that cannot be explained by Bogoliubov theory.

Strukturbildung in einem antiferromagnetischen Spinor Bose-Einstein Kondensat nach schneller Parameteränderung

In dieser Arbeit untersuchen wir Strukturbildung nach einer schnellen Änderung der Verstimmung der Spinaustauschwechselwirkung. Dafür verwenden wir ein effektives Spin-1 ^{87}Rb Bose-Einstein Kondensat in einer eindimensionalen Fallengeometrie. In bestimmten Regimen sagt Bogoliubovtheorie instabile Impulsmoden vorher. Diese werden durch spinaustauschende Stöße besetzt und die entstehende Struktur kann in transversaler Spinrichtung beobachtet werden.

Wir stellen unser experimentelles System vor und diskutieren die Parameter. Mit Hilfe zweier Analysemethoden, den Fourier Spektren des Spins und der räumlichen Korrelationsfunktion, vergleichen wir die experimentellen Resultate mit der homogenen Bogoliubovtheorie für kurze Evolutionszeiten. Die charakteristische Strukturgröße folgt den theoretischen Vorhersagen. Weiterhin diskutieren wir längere Evolutionszeiten, zu denen die Bogoliubovapproximation nicht mehr gültig ist. Das beobachtete Verhalten kann zum Teil durch eine veränderte Wechselwirkungsstärke, welche durch die Verminderung der kondensierten Mode bedingt ist, verstanden werden. Wir sehen erste Indikationen für entstehende Strukturen, die nicht mit Hilfe von Bogoliubovtheorie erklärt werden können.

Contents

1	Introduction	1
2	Theoretical Concepts	2
2.1	Spin Rotations	2
2.2	Hamiltonian	6
2.3	Mean-Field Ground State Diagram	8
2.4	Bogoliubov Theory	8
3	Experimental Manipulation Techniques	14
3.1	Experimental System	14
3.2	Imaging a Spinor Bose-Einstein Condensate	16
3.3	Magnetic Field Control	16
3.3.1	Magnetic Offset Field	16
3.3.2	Microwave Dressing	16
3.3.3	Spatial Gradients	19
3.4	Experimental Sequence	19
3.5	Experimental Observables for Detecting Spin Structures	21
4	Spin Exchange Dynamics and Growth Rate	23
4.1	Time Evolution	23
4.2	Calibrating the Fourier Transform	23
4.3	Measuring the Growth Rate	24
5	Structure Formation in a Spin-1 BEC	27
5.1	Short Time Evolution of the Fourier Spectra	27
5.1.1	What Are Short Times?	27
5.2	The Cut-Off Frequency	29
5.3	Extracting Structure Sizes	30
5.4	Comparing Short Times to Bogoliubov Theory	33
5.5	Beyond the Short Time Approximation	36
6	Conclusion and Outlook	42
	References	43
	Acknowledgement	45
	Declaration	46

1 Introduction

Ultracold atoms offer a high degree of experimental control and a large variety of techniques for their manipulation and probing. With this, they are ideal candidates for studying complex many-body physics, which is not easily accessible by classical computational simulations [1]. As the samples are cold and dilute, they offer a clean realization of the idealistic Hamiltonian and the isolation from the environment gives access to long coherent evolution times.

Theoretically, it is interesting whether and how such a system evolves to a new ground state after a quench of the Hamiltonian parameters [2, 3], in different regions of the related parameter space, such that the initial state gets unstable. To get a more intuitive feeling, imagine a potential of the form $V(x) = ax^2 + bx^4$. For positive a and b this is an anharmonic oscillator and $x = 0$ is the ground state. However, quenching to negative a we end up with the paradigmatic double well potential. Neglecting fluctuations, the system prepared at $x = 0$ is in a quasi-steady state. Even for $T = 0$ the system is unstable in this situation due to quantum fluctuations around its mean value $\langle x \rangle$. In a classical picture this corresponds to small displacements, which are amplified by the instability. As for the inverted pendulum, we will not find harmonic but hyperbolic solutions which lead to exponential acceleration away from $x = 0$. If there are processes allowing for the dissipation of energy it may reach the new ground state which is located in the minima of the double well.

In our experimental system such an instability can be introduced by spin-changing collisions [4]. For a Bose-Einstein condensate (BEC) prepared in a single hyperfine state $|F = 2, m_F = 0\rangle$ the total magnetization is a conserved quantity. However, processes populating $m_F = \pm 1$ in a correlated fashion are still possible but energetically suppressed by a detuning introduced by the second-order Zeeman shift in a magnetic field. In a one-dimensional confinement, we have not only the spin but also a spatial degree of freedom. Depending on the detuning specific spatial modes get unstable and grow exponentially. This leads to transient structure formation in the transversal spin [5].

This thesis is structured as follows: In chapter 2 we introduce the theoretical concepts. We discuss the related mean-field phase diagram and elucidate the calculations to obtain a dispersion relation in the Bogoliubov approximation. This is followed by a detailed description of the experimental system in chapter 3, where we discuss the control of the relevant experimental parameters. In chapter 4 we present the results obtained in the longitudinal spin direction. We show how we can map amplitudes in the Fourier spectra to occupation numbers. In chapter 5 we quantitatively compare the experimental results of the transversal spin to the theoretical predictions. We conclude with an outlook on future improvements and how we want to pursue.

2 Theoretical Concepts

In this first part, we want to have a look at the underlying theoretical concepts. We will start with some spin algebra to elucidate the connection between spin-1 and spin-2 systems in our situation. Second, we will look at the Hamiltonian describing a spinor BEC. The non-interacting and the interacting part will be described in detail and we will discuss the accessible phase diagram. In the experimental sequence, we quench a parameter of the Hamiltonian in different regimes. To understand the dynamics we can expand our Hamiltonian in the fluctuations for short times around a highly occupied state and will end up with the well-known Bogoliubov theory [6]. It predicts unstable modes which are expected to grow exponentially for short times.

2.1 Spin Rotations

In ^{87}Rb we can choose between a spin-1 and a spin-2 system depending on the choice of the hyperfine manifold. All experiments described in this thesis are done in the $F = 2$ manifold, i.e. we are dealing with a spin-2 system. As we will see later the $m_F = \pm 2$ states are far detuned for spin-mixing processes and the population in these states will therefore be negligible. Thus, we would like to map the spin-2 to an effective spin-1 system, which makes the calculations much easier.

For spin-1 we can write the spin matrices as [7]

$$F_x = \frac{1}{\sqrt{2}} \begin{pmatrix} 0 & 1 & 0 \\ 1 & 0 & 1 \\ 0 & 1 & 0 \end{pmatrix} \quad F_y = \frac{i}{\sqrt{2}} \begin{pmatrix} 0 & -1 & 0 \\ 1 & 0 & -1 \\ 0 & 1 & 0 \end{pmatrix} \quad F_z = \begin{pmatrix} 1 & 0 & 0 \\ 0 & 0 & 0 \\ 0 & 0 & -1 \end{pmatrix}. \quad (1)$$

We now want to calculate the expectation value $\langle \Psi | F_i | \Psi \rangle$ of the spin matrices for a general spinor $\Psi = (\Psi_{+1}, \Psi_0, \Psi_{-1})^T$, where $\Psi_{0,\pm 1}$ are complex numbers. We end up with

$$\langle F_x \rangle = \frac{1}{\sqrt{2}} [(\Psi_1^* + \Psi_{-1}^*) \Psi_0 + \Psi_0^* (\Psi_1 + \Psi_{-1})] \quad (2)$$

$$\langle F_y \rangle = \frac{i}{\sqrt{2}} [(\Psi_{-1}^* - \Psi_1^*) \Psi_0 + \Psi_0^* (\Psi_1 - \Psi_{-1})] \quad (3)$$

$$\langle F_z \rangle = |\Psi_1|^2 - |\Psi_{-1}|^2 \quad (4)$$

To compare these results to the expectation value for the spin-2 case we will use the

same spinor but extended to five states. Again we can write the spin matrices as

$$\begin{aligned}
F_x &= \begin{pmatrix} 0 & 1 & 0 & 0 & 0 \\ 1 & 0 & \sqrt{\frac{3}{2}} & 0 & 0 \\ 0 & \sqrt{\frac{3}{2}} & 0 & \sqrt{\frac{3}{2}} & 0 \\ 0 & 0 & \sqrt{\frac{3}{2}} & 0 & 1 \\ 0 & 0 & 0 & 1 & 0 \end{pmatrix} & F_y &= \begin{pmatrix} 0 & -i & 0 & 0 & 0 \\ i & 0 & -i\sqrt{\frac{3}{2}} & 0 & 0 \\ 0 & i\sqrt{\frac{3}{2}} & 0 & -i\sqrt{\frac{3}{2}} & 0 \\ 0 & 0 & i\sqrt{\frac{3}{2}} & 0 & -i \\ 0 & 0 & 0 & i & 0 \end{pmatrix} \\
F_z &= \begin{pmatrix} 2 & 0 & 0 & 0 & 0 \\ 0 & 1 & 0 & 0 & 0 \\ 0 & 0 & 0 & 0 & 0 \\ 0 & 0 & 0 & -1 & 0 \\ 0 & 0 & 0 & 0 & -2 \end{pmatrix}.
\end{aligned} \tag{5}$$

Assuming that there is no population in the $m_F = \pm 2$ states we can write the spin-2 spinor as $\Psi = (0, \Psi_{+1}, \Psi_0, \Psi_{-1}, 0)^T$. As a first example, we calculate the expectation value of the F_z matrix with $\langle \rangle_{F=f}$ being the expectation value of the spin-f matrix for the spin-f spinor

$$\langle F_z \rangle_{F=2} = |\Psi_1|^2 - |\Psi_{-1}|^2 \propto \langle F_z \rangle_{F=1}. \tag{6}$$

So we see that the expectation value of the spin-2 system is the spin-1 expectation. Experimentally this expectation value is well accessible as the population of the two spin states is directly measured by absorption imaging. However, for calculating the F_x or F_y spin we need the complex wavefunction or have to image in another direction relative to the magnetic field. Instead, we rotate the spin by radio frequency magnetic fields by a $\pi/2$ rotation, such that the spin component is mapped on to the the z - direction, i. e. our imaging direction. We do only one pulse, so the rotation axis is not defined because only relative phases are defined. Our initial state has no distinct direction and we have a rotational symmetry around the z -axis such that we can choose F_x as our rotation axis.

Spin-1 Sphere

To get a more intuitive feeling for these rotations, we introduce at this point the spin-1 sphere. It is a sphere of radius 1 where the axes are given by the expectation values of the three spin matrices. A single spin of length 1 can be decomposed into two spin-1/2. As we want to have a spin with spin length one, we look at the symmetric superposition as basis vectors. The spin triplet is given as

$$\begin{pmatrix} 1 \\ 0 \\ 0 \end{pmatrix} = |\uparrow\uparrow\rangle \quad \begin{pmatrix} 0 \\ 0 \\ 1 \end{pmatrix} = |\downarrow\downarrow\rangle \quad \begin{pmatrix} 0 \\ 1 \\ 1 \end{pmatrix} = \frac{1}{\sqrt{2}} (|\uparrow\downarrow\rangle + |\downarrow\uparrow\rangle). \tag{7}$$

We now want to look at uncertainties of the state $|\Psi\rangle_{polar} = (0, 1, 0)^T$, which we will call **polar state**. The uncertainties are calculated with the earlier introduced spin-1

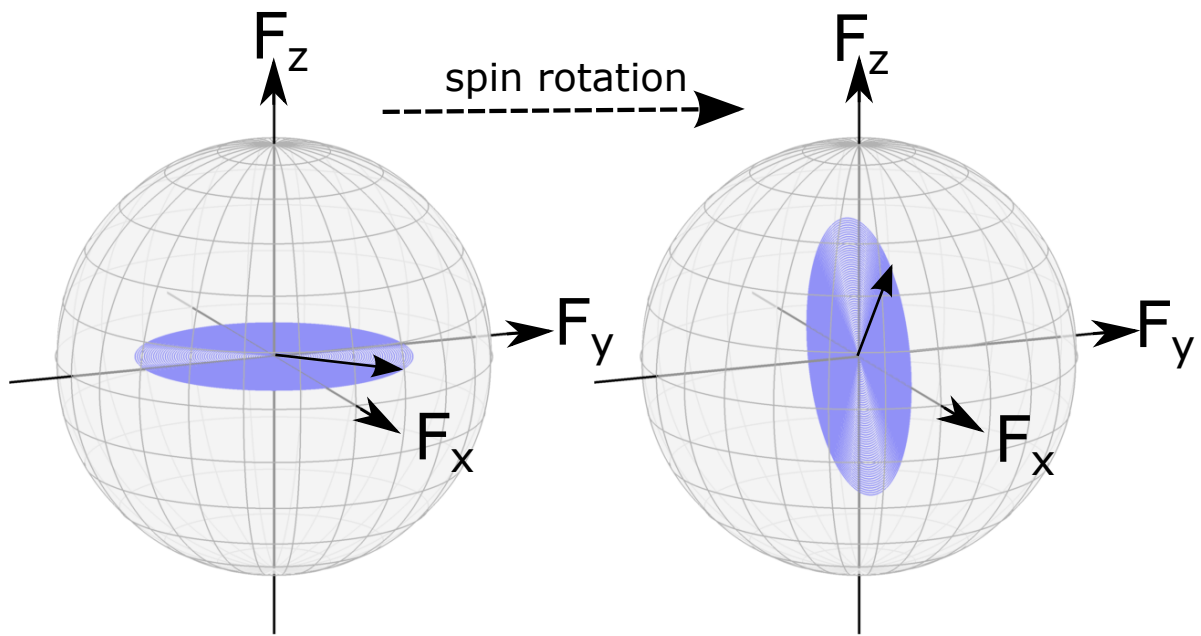


Figure 1: **N particle spin-1 sphere** Here the spin-1 sphere for 10 particles is shown. The blue disc represents a polar coherent state. After a $\pi/2$ rotation around the F_x axis the disc is rotated into the x-y-plane and potentially contained structure can be imaged by imaging the F_z spin. The black arrow is for better orientation in the three dimensional plot and represents an arbitrary spin direction.

matrices as

$$\begin{aligned}\langle \Delta F_x^2 \rangle_{polar} &= \langle \Psi | F_x^2 | \Psi \rangle_{polar} - \langle \Psi | F_x | \Psi \rangle_{polar}^2 = 1 \\ \langle \Delta F_y^2 \rangle_{polar} &= 1 \\ \langle \Delta F_z^2 \rangle_{polar} &= 0.\end{aligned}\tag{8}$$

For a general spin direction $F_\phi = \cos \phi F_x + \sin \phi F_y$ we find

$$\langle \Delta F_\phi \rangle_{polar} = 1.$$

So the single spin in this state can be represented in the spin-1 sphere as a disc in the x-y-plane with radius $\sqrt{1}$.

This is generalized to N spin-1 particles that we can represent as a single spin with length N if we add up all spins symmetrically. As all particles are identical, we can write

$$|\Psi\rangle_{polar} \longrightarrow \begin{pmatrix} 0 \\ 1 \\ 0 \end{pmatrix}^{\otimes N} \quad \text{and} \quad F_i \longrightarrow F_i^{\otimes N},$$

then variances add up linearly and we end up with

$$\begin{aligned}\langle \Delta F_x^2 \rangle &= \langle \Delta F_y^2 \rangle = N \\ \langle \Delta F_z^2 \rangle &= 0.\end{aligned}\tag{9}$$

So the initial state of all experiments carried out in this thesis is a disc with width \sqrt{N} in the x-y-plane.

The F_i matrices are the generators of a rotation in spin space, where a generic rotation is given by

$$\mathcal{R}_\tau^{F_i} = e^{-iF_i\tau}.\tag{10}$$

In the experiment we choose $\tau = \pi/2$. The rotation matrix is

$$\mathcal{R}_{\frac{\pi}{2}}^{F_x} = \begin{pmatrix} \frac{1}{4} & -\frac{i}{2} & \frac{\sqrt{6}}{4} & \frac{i}{2} & \frac{1}{4} \\ -\frac{i}{2} & \frac{1}{2} & 0 & -\frac{1}{2} & \frac{i}{2} \\ -\frac{\sqrt{6}}{4} & 0 & -\frac{1}{2} & 0 & -\frac{\sqrt{6}}{4} \\ \frac{i}{2} & -\frac{1}{2} & 0 & -\frac{1}{2} & -\frac{i}{2} \\ \frac{1}{4} & \frac{i}{2} & \frac{\sqrt{6}}{4} & -\frac{i}{2} & \frac{1}{4} \end{pmatrix}.\tag{11}$$

The rotated state is

$$\Psi_{rot} = \mathcal{R}_{\frac{F_x}{2}} \Psi = \begin{pmatrix} -\frac{i}{2}\Psi_1 + \frac{\sqrt{6}}{4}\Psi_0 + \frac{i}{2}\Psi_{-1} \\ -\frac{1}{2}(\Psi_1 - \Psi_{-1}) \\ -\frac{1}{2}\Psi_0 \\ -\frac{1}{2}(\Psi_1 - \Psi_{-1}) \\ \frac{i}{2}\Psi_1 + \frac{\sqrt{6}}{4}\Psi_0 - \frac{i}{2}\Psi_{-1} \end{pmatrix}. \quad (12)$$

Experimentally we can only detect densities. However the expectation value of F_z can now easily be calculated from the densities, see eq. (6), as being

$$\langle \Psi_{rot} | F_z | \Psi_{rot} \rangle_{F=2} = i \frac{\sqrt{6}}{2} [(\Psi_{-1}^* - \Psi_1^*) \Psi_0 + \Psi_0^* (\Psi_1 - \Psi_{-1})] \propto \langle F_x \rangle_{F=1}. \quad (13)$$

The calculation is done similarly for any other spin direction lying in the x-y-plane.

We are here dealing with a spin-2 system with negligible population of the $m_F = \pm 2$, do a spin rotation including all 5 states and calculate the true spin-2 spin in z-direction. However, we have shown with this calculation, that we can describe the system as effectively being spin-1. This simplifies the Hamiltonian significantly.

Now we are going on by introducing the Hamiltonian of the spin-1 system to describe the mean field phase diagram and the dynamics out of equilibrium. By comparing to the full spin-2 theory we will find out how to modify the interaction constants. However, we want to mention here, that also experiments using the full spin length of 2 [8, 9] and exploring spin-2 distinct nematic phases [10] have been carried out.

2.2 Hamiltonian

In this part, we will introduce the non-interacting and the interacting part of the Hamiltonian and discuss all terms in detail. For the description we use field operators $\hat{\psi}_m(\vec{r})$, with $m = \pm 1, 0$, which obey the standard bosonic commutation relation.

Non-interacting Part

The non-interacting part can be divided into three parts. The kinetic energy and the trapping potential, as well as the shift introduced by the magnetic field. In second quantized form we can write the Hamiltonian as

$$\hat{H}_0 = \int d\vec{r} \sum_{m,m'=-f}^f \hat{\psi}_m^\dagger(\vec{r}) \left[-\frac{\hbar \nabla^2}{2m} + U_{\text{trap}}(\vec{r}) - p(F_z)_{mm'} + q(F_z^2)_{mm'} \right] \hat{\psi}_{m'}(\vec{r}). \quad (14)$$

$(F_z)_{mm'}$ are the entries of the F_z spin matrix. The term proportional to p represents the linear Zeeman shift. As the interaction is on the order of Hz we cannot neglect the second order Zeeman shift. The constant q can be calculated with the Breit-Rabi formula [11] as

$$q = \frac{(g\mu_B)^2}{\Delta E_{\text{hfs}}} \approx 72 \frac{\text{Hz}}{\text{G}^2} B^2,$$

with μ_B being the Bohr magneton and $g = 1/2$ the g-factor and B the magnetic field strength. The hyperfine splitting is $\Delta E_{\text{hfs}} \approx 6.8$ GHz for the ground state of ^{87}Rb . Later we will introduce microwave dressing as a tool to tune the energy mismatch.

Interacting Part

The interaction part is given by collisional interactions between the different states that can change the spin state of the colliding particles. As we are here dealing with a dilute sample of particles we are only considering binary collisions. The many body wave function changes by a factor of $(-1)^{\mathcal{F}+\mathcal{L}}$ under the exchange of two identical particles. For temperature well below the condensation temperature we can restrict ourselves to s-wave scattering, i. e. $\mathcal{L} = 0$. Therefore, the total spin of the two colliding particles \mathcal{F} has to be even, which allows for spin-1 the scattering channels $\mathcal{F} = 0, 2$.

The full derivation of the interaction Hamiltonian can be found here [7]. For our purposes we just define it as

$$\hat{V} = \frac{1}{2} \int d\vec{r} \left[c_0 : \hat{n}^2 : + c_1 : \hat{\mathcal{F}}^2 : \right]. \quad (15)$$

which we can divide [12] in the symmetric part proportional to c_0 and the anti-symmetric part proportional to c_1 and $::$ indicates normal ordering. The interaction strengths for $\mathcal{F} = 2$ are given by

$$c_0 = \frac{4g_2 + 3g_4}{7} \quad c_1 = \frac{g_4 - g_2}{7}, \quad (16)$$

where $g_i = \frac{4\pi\hbar^2 a_i}{m}$ with a_i being the scattering length of the spin channel i . The symmetric part does not change the spin states of the involved particles.

To see the action of the anti-symmetric term we explicitly factorize it,

$$c_1 : \hat{\mathcal{F}}^2 : = c_1 : \left[\left(\hat{\psi}^\dagger \hat{F}_x \hat{\psi} \right)^2 + \left(\hat{\psi}^\dagger \hat{F}_y \hat{\psi} \right)^2 + \left(\hat{\psi}^\dagger \hat{F}_z \hat{\psi} \right)^2 \right] :. \quad (17)$$

and $\psi = (\psi_{+1}, \psi_0, \psi_{-1})^T$ the spinor of the field operators.

$$\hat{\mathcal{H}}_{as} = 2c_1 \left(\psi_{+1}^\dagger \psi_{-1}^\dagger \psi_0 \psi_0 + h.c. \right) + 2c_1 \hat{N}_0 \left(\hat{N}_{+1} + \hat{N}_{-1} \right) + c_1 \left(\hat{N}_{+1} - \hat{N}_{-1} \right)^2 \quad (18)$$

where we have neglected constant shifts proportional to the total atom number and we introduced $\hat{N}_i = \hat{\psi}_i^\dagger \hat{\psi}_i$. The first term gives rise to spin-changing collisions (SCC) [4]. Two atoms in $m_F = 0$ (pump mode) are annihilated and each one atom in $m_F = \pm 1$ (side modes) is created. The interaction strength is characterised by the scattering length difference c_1 and the detuning of the process is given by the second order Zeeman shift, i. e. by the magnetic field. The process leads to squeezing of the side mode population difference and is similar to parametric down conversion in optics, which leads to the two-mode squeezed vacuum state [13]. The second term causes an energy shift of the states proportional to

their population. The last term leads to the formation of spin domains for negative c_1 , so in $F=1$ for ^{87}Rb . Local population imbalance, i. e the generation of spin makes this term grow.

Knowing the general structure of the Hamiltonian we can go on with discussing the mean field ground states. These can easily be found by looking at the energy functional.

2.3 Mean-Field Ground State Diagram

As we are interested in non-equilibrium dynamics we are first interested in the ground state of our system. Knowing that, we can prepare a certain state we can quench a parameter of the Hamiltonian, in our case the detuning of the SCC q . This will lead to an unstable system and exponentially growing occupation numbers for certain modes as we will see in the next chapter about Bogoliubov theory.

We can find the mean field ground state by looking at the energy per particle. It is obtained by the expectation value of the Hamiltonian as described in [7], while neglecting the kinetic energy

$$\epsilon = \sum_m qm^2 |\xi_m|^2 + \frac{1}{2}c_0n + \frac{1}{2}c_1n|\mathbf{f}|^2, \quad (19)$$

where ξ_m ($m = 0, \pm 1$) is a normalized spinor and n the number density. \mathbf{f} is the spin expectation value per particle. Furthermore, we neglect the term $\propto pF_z$ as we prepare a state with no mean magnetization and the magnetization is conserved by the Hamiltonian.

Here we only discuss the case $c_1 > 0$ as this is the case for $F = 2$ in ^{87}Rb what is subject of this thesis. For $q > 0$ the **polar state** $(0, 1, 0)^T$ is the ground state, as the spin length equal to zero minimizes the mean field energy. For $q < 0$ the ground state has also no mean spin length but we can lower the energy by populating the $m_F = \pm 1$ states. We are in the **transverse polar phase** and the ground state is a $\pi/2$ rotation around F_x of the polar state $\psi_{\text{tp}} = \frac{1}{\sqrt{2}}(1, 0, 1)^T$. In Fig. 2 the situation is schematically shown. For $q > 0$ the SCC are tuned out of resonance. Preparing the polar state and quenching to $q < 0$ we are not in the ground state any more. In the next section we are going to explore the structure contained in the, as grey shaded boxes depicted, side modes.

2.4 Bogoliubov Theory

For a one-component BEC we can expand the interacting Hamiltonian around the highly occupied Bose condensed $k = 0$ state. Expanding up to second order in the fluctuations we can find a transformation which diagonalizes the Hamiltonian, the Bogoliubov transformation [14]. These corresponding quasi-particles give us a phonon dispersion relation up to the healing length momentum and the quantum depletion [15].

We now want to do the same for the spin-1 Hamiltonian to find the excitations in the different q regimes. Expanding around the polar state we find a stable BEC for $q > 0$ with only phononic excitation. However, for q the BEC gets unstable as the dispersion relation becomes imaginary and we get exponentially growing occupation numbers. This is due to the fact, that we quench into a region with a different mean-field ground state.

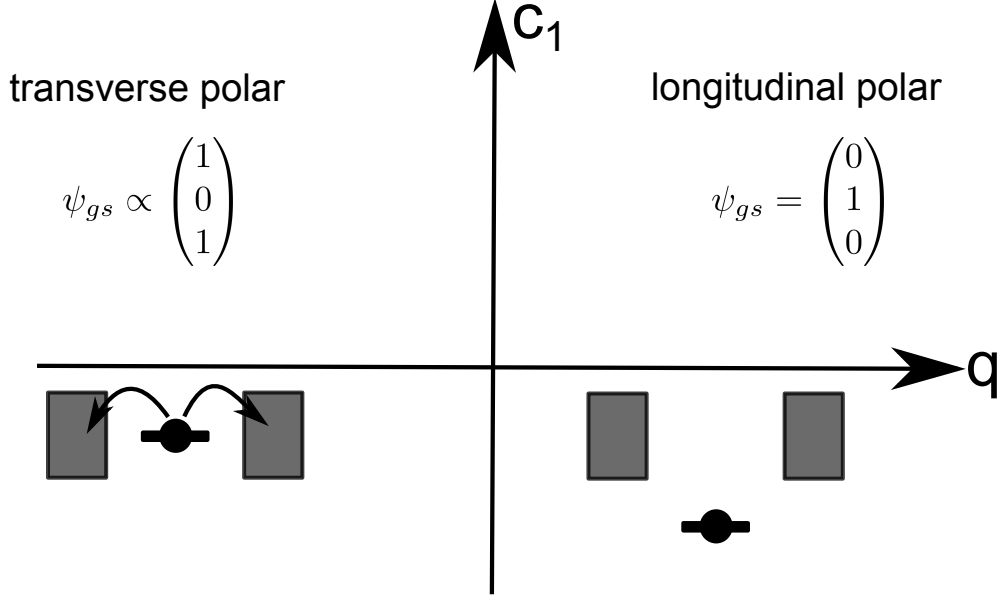


Figure 2: **Phase diagram for the spin-1 BEC** In the phase diagram we use as parameters the interaction strength c_1 and the second order Zeeman shift q . For $F = 2$ c_1 is positive. We have two different phases for the different signs of q , which are separated by a first order phase transition. The sketch in the lower half is depicting the single particle energy levels. For $q < 0$ the pump mode (black) is energetically higher than the side modes (grey boxes) and spin-changing collisions are tuned into resonance.

We will describe the steps to get the simplified Hamiltonian for the spin-changing part of the interaction. We can only completely solve this analytically for $V(\vec{r}) = \text{const.}$, i. e. a spatially homogeneous situation. In the following we will write operators without using a hat. We write

$$\mathcal{H}_{\text{int}}^{(2)} = c_1 \int dx \left[2\psi_0^\dagger \psi_0 \left(\psi_1^\dagger \psi_1 + \psi_{-1}^\dagger \psi_{-1} \right) + 2 \left(\psi_1^\dagger \psi_{-1}^\dagger \psi_0 \psi_0 + h.c. \right) \right]. \quad (20)$$

We then expand the field operator in plane waves

$$\psi_i = \frac{1}{\sqrt{V}} \sum_k a_{k,i} e^{ikx} \quad (21)$$

with $a_{k,i}$ being the annihilation operator of an particle in the state $i = m_F = \pm 1$ with momentum k and insert equation (21) in (20) and end up with:

$$\begin{aligned} \mathcal{H}_{\text{int}}^{(2)} = & \frac{2c_1}{V^2} \int dx \sum_{k,p,q,m} \left[\left(a_{p,0}^\dagger a_{m,1}^\dagger a_{k,0} a_{q,1} + a_{p,0}^\dagger a_{m,-1}^\dagger a_{k,0} a_{q,-1} \right) e^{-ix(p+m-k-q)} \right. \\ & \left. + \left(a_{p,1}^\dagger a_{m,-1}^\dagger a_{k,0} a_{q,0} + h.c. \right) e^{-ix(q+m-k-p)} \right] \end{aligned} \quad (22)$$

Obeying momentum conservation by using an identity for the delta distribution

$$\delta_{kk'} = \frac{1}{V} \int dx e^{ix(k-k')}$$

we can eliminate the summation over m and restrict ourselves to processes of the form

$$k + q \rightarrow p + p_2$$

with $p_2 = (-p + k + q)$.

We get

$$\mathcal{H}_{\text{int}}^{(2)} = \frac{2c_1}{V} \sum_{k,q,p} \left[\left(a_{p,0}^\dagger a_{p_2,1}^\dagger a_{k,0} a_{q,1} + a_{p,0}^\dagger a_{p_2,-1}^\dagger a_{k,0} a_{q,-1} \right) + \left(a_{p,1}^\dagger a_{p_2,-1}^\dagger a_{k,0} a_{q,0} + h.c. \right) \right] \quad (23)$$

We initially prepare a BEC in the $m_F = 0$ state, therefore we are dealing with a highly occupied momentum $k = 0$ in this state. In the limit that the depletion due to the dynamics is negligible compared to the initial size we write the operators $a_{0,0}^{(\dagger)}$ as complex numbers by writing

$$a_{0,0}^{(\dagger)} = \sqrt{N} \quad (24)$$

with N being the total number of particles. Expanding the Hamiltonian in eq. 20 up to second order in the other annihilation and creation operators we get the final form

$$\mathcal{H}_{\text{int}}^{(2)} = 2nc_1 \sum_k \left[\left(a_{k,1}^\dagger a_{k,1} + a_{k,-1}^\dagger a_{k,-1} \right) + \left(a_{k,1}^\dagger a_{-k,-1}^\dagger + h.c. \right) + \mathcal{O}(a^4) \right] \quad (25)$$

with $n = \frac{N}{V}$ being the particle density.

We proceed with the other two parts of the Hamiltonian in the same way, this is not shown here but can be calculated in the same way as the example showed here. For the second part of the interaction Hamiltonian we get

$$\mathcal{H}_{\text{int}}^{(1)} = c_0 \int dx : n^2 := 2nc_0 \sum_k \left(a_{k,1}^\dagger a_{k,1} + a_{k,0}^\dagger a_{k,0} + a_{k,-1}^\dagger a_{k,-1} \right) + 2nc_0 N + \mathcal{O}(a^4). \quad (26)$$

Finally the non-interacting part can be written as

$$\mathcal{H}^{(0)} = \sum_k \sum_{m_F} (\epsilon_k + m_F^2 q) a_{k,m_F}^\dagger a_{k,m_F}. \quad (27)$$

The resulting Hamiltonian is not diagonal in the original annihilation (creation) operators. The goal is to find a new basis diagonalizing the Hamiltonian and simultaneously revealing the dispersion relation for the quasi particle modes. We make the following ansatz

$$b_{k,i} = u_{k,i}a_{k,i} - v_{k,i}^*b_{-k,i}^\dagger \quad (28)$$

with $b_{k,i}^{(\dagger)}$ being the quasi particle annihilation (creation) operators and $u_{k,i}$ the mode functions. $b_{k,i}^{(\dagger)}$ should obey the normal commutation relation $[b_{k,i}, b_{q,j}^\dagger] = \delta_{kq}\delta_{ij}$ and so we get a condition for the mode functions

$$|u_{k,i}|^2 - |v_{k,i}|^2 = 1$$

which shows us that the transformation has to be symplectic. The transformation is called **Bogoliubov transformation** [6] and we end up with a Hamiltonian of the form

$$\mathcal{H} = \sum_i \hbar\omega_{k,i}b_{k,i}^\dagger b_{k,i} + \text{const.} \quad (29)$$

For the $m_F = 0$ state we get the typical density excitations giving the phonon dispersion relation for low k like in a single component BEC:

$$\omega_{k,0} = \sqrt{\epsilon_k (\epsilon_k + 2nc_0)} \quad (30)$$

$$b_{k,0} = \sqrt{\frac{\epsilon_k + nc_0 + E_{k,0}}{2E_{k,0}}}a_{k,0} + \sqrt{\frac{\epsilon_k + nc_0 - E_{k,0}}{2E_{k,0}}}a_{k,0}^\dagger \quad (31)$$

The meaning of this will be discussed in a few lines. First we want to have a look at the excitation in the side modes

$$\omega_{k,\pm 1} = \sqrt{(\epsilon_k + q)(\epsilon_k + q + 2nc_1)} \quad (32)$$

$$b_{k,\pm 1} = \sqrt{\frac{\epsilon_k + q + nc_1 + E_{k,\pm 1}}{2E_{k,\pm 1}}}a_{k,\pm 1} + \sqrt{\frac{\epsilon_k + q + nc_1 - E_{k,\pm 1}}{2E_{k,\pm 1}}}a_{k,\pm 1}^\dagger \quad (33)$$

We have seen in eq. 2 and 3 that we can write the spin in x(y)-direction as the (anti)symmetric superposition of the side mode operators. In our case, the two Bogoliubov modes for $m_F = \pm 1$ are degenerated. Thus, every linear superposition is again an eigenvector of the corresponding Bogoliubov-de Gennes equations. So let us introduce two new modes as

$$b_{k,F_x} \propto b_{k,1} + b_{k,-1} \quad (34)$$

$$b_{k,F_y} \propto i(b_{k,1} - b_{k,-1}) \quad (35)$$

These correspond to excitations in the transversal spin direction. They can experimentally be revealed by the explained spin rotations and are used in the following.

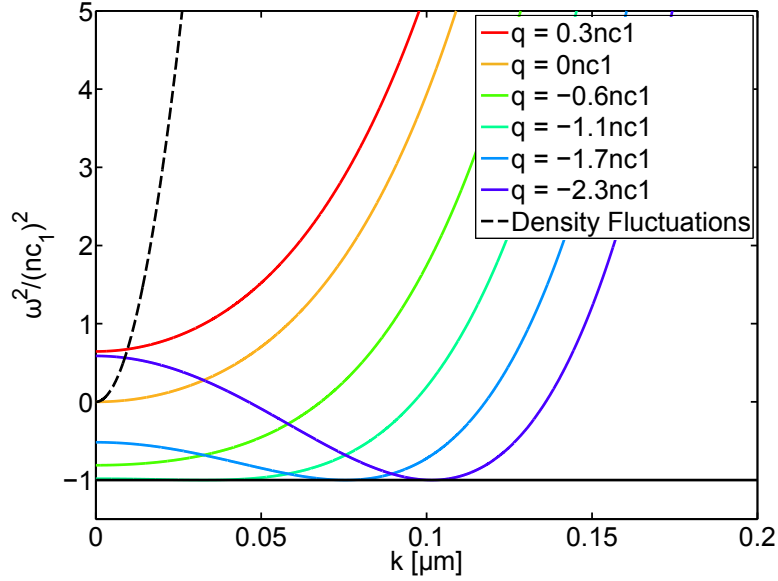


Figure 3: **Dispersion relation of the modes found by Bogoliubov transformation** The colored solid lines show the squared dispersion relation of the spin fluctuation modes, eq. 34 and 35. For $q > 0$ the dispersion relation is gapped with a gap $\sqrt{q(q + nc_1)}$. For $q < 0$ some k modes are unstable as the squared dispersion becomes negative which lead to an exponential growth of the occupation. We identify three different regime. For $-nc_1 < q < 0$ the most unstable mode is $k = 0$ and the growth rate is growing up to $q = -nc_1$. A finite k is most unstable for $q < -nc_1$ and the growth rate is constant nc_1 . In the regime $q < -2nc_1$ the $k = 0$ is not unstable anymore.

Now let us discuss the currently introduced dispersion relations. In Fig. 3 the dispersion relation of the density (black dashed line) as well as the spin fluctuations (color lines) are shown. The density fluctuations have a linear dispersion relation up to the inverse healing length $\xi^{-1} = \sqrt{2mc_0n}/\hbar$, corresponding to phononic excitations [15]. Above ξ^{-1} we have particle excitations and a quadratic dispersion relation.

The dispersion relation of the spin fluctuations is depending on the SCC detuning q . For $q > 0$ we have a gapped dispersion relation with a gap $\sqrt{q(q + nc_1)}$. For $q < 0$ we get k modes with negative ω^2 , i. e. the modes become unstable. This we can see by looking at the phase evolution $\propto e^{-i\omega t}$, which gives an exponential growth for a non-zero imaginary part of ω . In the unstable regime the made approximation is only valid for short times, as due to the exponential growth the approximation of the non depleted zero mode is not valid any more eventually. Now let us look at the most unstable mode, i. e. the mode with the largest imaginary part. In the regime $-nc_1 < q < 0$ the most unstable mode is $k = 0$ with growth rate up to $q = nc_1$ where the growth rate is nc_1 . In the regime $q < -nc_1$ the most unstable mode is given by

$$k_{\text{mu}} = \sqrt{-\frac{2m}{\hbar}(q + nc_1)}, \quad (36)$$

where k is given as an inverse wavelength $1/\lambda$ and q and nc_1 in Hz. The growth rate is constant and equal to nc_1 . A third regime is defined by $q < -2nc_1$, as from here on the lowest k modes are stable. In the last part of this theses we compare these expectations to the experimental results.

As a last point we have to discuss how we have to adjust the interaction strength c_1 to account for our approximation of a spin-1 system. In a spin-2 system we would also have to introduce a further interaction

$$c_2 = \frac{7g_0 - 10g_2 + 3a_4}{35}$$

allowing for processes $0, 0 \rightarrow +2, -2$. Doing the full Bogoliubov theory leads to the similar modes introduced in equation (30) and (32) for $m_F = \pm 1$, but the dispersion relation is modified due to interactions described by c_2

$$\omega_{k,\pm 1} = \sqrt{(\epsilon_k + q)(\epsilon_k + q + 2n(3c_1 - c_2/5))}. \quad (37)$$

Thus we have to adjust the interaction appearing in the dispersion relation as follows

$$c_1 \rightarrow 3c_1 - c_2/5. \quad (38)$$

This leads to an about three times larger interaction as expected from the simple spin-1 approximation.

We now have everything at hand to understand the following discussion about the dynamics happening in the experiment and will now go on with a discussion of the experimental setup.

3 Experimental Manipulation Techniques

In the first chapter we described the Hamiltonian of a spinor BEC. We now want to look at the experimental implementation and the readout of the final state after the time evolution. First, we describe the spatial confinement and the typical energy scales. We characterize the magnetic field and the microwave dressing used to change the parameter q , describing the energy mismatch between the pump and the side modes. In the end, we discuss how to access the growing modes of the transversal spin experimentally.

3.1 Experimental System

We routinely produce a ^{87}Rb condensates confined in a weakly focussed far off-resonant laser beam, which realizes a dipole trap with a high aspect ratio with trap frequencies of $\omega_{\parallel} = 2\pi \times 2.6 \text{ Hz}$ in the longitudinal direction and $\omega_{\perp} = 2\pi \times 260 \text{ Hz}$ in the transversal direction. In the Thomas-Fermi approximation [15] the kinetic energy of the condensate is neglected and we get a formula for the density profile of the cloud

$$n(x) = \frac{\mu - V(x)}{g}, \quad (39)$$

where $V(x) = 1/2m\omega^2x^2$ is the trapping potential. For ^{87}Rb in $F = 2$ the density interaction constant is $c_0 = 95.9a_B$ [4]. With μ we introduced the chemical potential, which corresponds to the interaction energy per particle of the BEC. The big aspect ratio of the trap of $\sim 1/100$ creates a quasi one-dimensional situation. The typical energy scales set by the chemical potential and the temperature, $\sim 10 \text{ nK}$, should not be much larger than the excitation energy in transversal direction. From eq. 39 we immediately get the chemical potential by

$$\mu = gn(0).$$

So it is given by the density in the center of the trap and the scattering interaction constant. We can, however, only measure linear densities in the longitudinal direction and therefore we have to adjust $g \rightarrow g/(2\pi a_{\perp}^2)$ with the harmonic oscillator length $a_{\perp} = \sqrt{\frac{\hbar}{m\omega_{\perp}}}$, to take into account the extension in transversal direction. Experimentally, $n(0)$ is determined by taking the mean linear density in the center of the trap. For this the sample is imaged after negligible evolution time. We find

$$\mu \approx 2\pi \times 500 \text{ Hz}$$

So the chemical potential is around twice the trapping frequency in longitudinal direction. However, we can compare the transversal extension $a_{\perp} = 0.6 \mu\text{m}$ to the spin healing length $\xi = \hbar/\sqrt{2mg\bar{n}}$ [16], where we take $ng = 2\pi \times 17.7 \text{ Hz}$ and m is the atomic mass of Rb. The spin interaction strength is in the last part determined from the excitation spectrum. The spin healing length gives the minimum size of possible spin excitations in the system, i. e. they are suppressed in transversal direction.

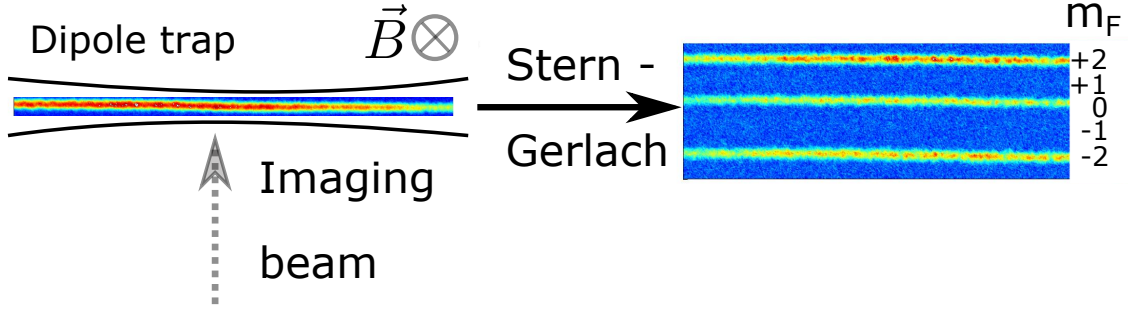


Figure 4: **Trapping and imaging a spinor BEC** The spinor BEC is trapped in a weakly focused dipole trap. The resonant imaging light is applied perpendicular to the magnetic field. A magnetic field gradient is applied after switching off the dipole trap to spatially separate the different magnetic sub-levels. The right panel shows an image of the rotated initial state.

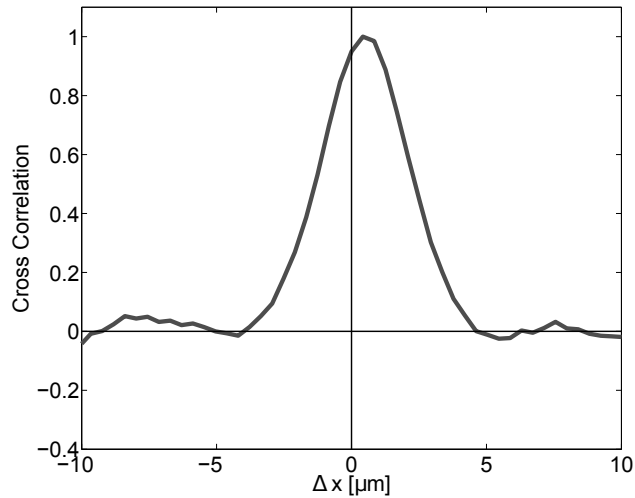


Figure 5: **Exemplary spatial cross correlation function of the $m_F = \pm 1$ component after $\pi/2$ - rf-rotation** For two equally centred profiles the maximum should be at $\Delta x = 0$. The shift of around $0.5 \mu\text{m}$ is probably due to a relative angle between magnetic field and the Stern-Gerlach direction. Compared to the typical domain size of $> 10 \mu\text{m}$ this shift does not affect the measured structure size on the level of the experimental accuracy.

3.2 Imaging a Spinor Bose-Einstein Condensate

To access the spin dynamics we have to access different spin components. For this, the gas is released from the trap after the experimental sequence and after a Stern-Gerlach pulse, a strong magnetic field gradient, following a short time of flight all five m_F -components are imaged by absorption imaging (see Fig. 4) [17] with a resolution of $\sim 1 \mu\text{m}$. If the gradient separating the atoms is not perfectly parallel to the magnetic field axis the m_F -components are shifted relative to each other. This could cause differences in the observed structure size. In 2.1 we have seen that the $m_F = \pm 1$ components should be perfectly symmetric after doing a $\pi/2$ rotation of a spin-2 state with no population in $m_F = \pm 2$ around F_x . Therefore, we can check the misalignment of the Stern-Gerlach by calculating the spatial cross correlation between $m_F = \pm 1$. In Fig. 5 we can see that the shift is about $0.5 \mu\text{m}$. This results in a shift smaller than $2 \mu\text{m}$ for the $m_F = \pm 2$ components, while the typical domain sizes are much larger. Thus it has no strong influence on the structure size on the level of the experimental detection accuracy.

Bogoliubov theory is predicting excitations in the x- and y- component of the spin. For imaging these we have to do a spin rotation. This is done by a radio frequency magnetic field coupling all five levels of the $F = 2$ manifold. The Hamiltonian describing this process is $\mathcal{H} \propto \Omega F_\phi$, with Ω being the Rabi frequency of the coupling. The coupling rotates a spin vector around a random axis in the x-y-plane in the generalized spin-1 sphere introduced earlier. Thus, experimentally we average over all angles $\phi \in [0, 2\pi]$. Exemplary, imaging the gas after a $\pi/2$ spin rotation around F_x , we map the F_y -component of the spin on the z-axis. As the Hamiltonian is rotationally symmetric and further the spin excitation in the x- and y-direction are degenerate the structure size emerging does not depend on the direction of the rotation.

3.3 Magnetic Field Control

3.3.1 Magnetic Offset Field

Well controlled magnetic fields in the experimental chamber are important, since the Hamiltonian describing the dynamics contains terms depending on the magnetic field.

The magnetic field results in an energy shift $\Delta E \propto m_F p B$ of the magnetic sublevels, with $p \approx 700 \text{ kHz/G}$, the linear Zeeman effect. The spin-changing collision process has no detuning due to the linear Zeeman effect and we therefore go into a rotating frame with Larmor frequency $\omega_L = 2\pi \times p B$. The energy eigenvalues for small magnetic field are well described by the linear and the second-order Zeeman shift. The Breit-Rabi formula [11] captures this effect. For the ground state in ^{87}Rb , we have $\Delta E_B = \pm(4 - m_F^2)qB^2$ with $q = 72 \text{ Hz/G}^2$. In the $F = 1$ manifold the pump mode is effectively shifted to a lower energy as the side modes, which we call positive detuning, and in $F = 2$ vice versa. The level scheme including the second order shift for $F = 2$ can be seen in Fig. 6.

3.3.2 Microwave Dressing

To quench in the different regimes of the phase diagram, we want to have experimental control over the detuning $q_B = qB^2$. Holding the offset field fixed, this can be done by

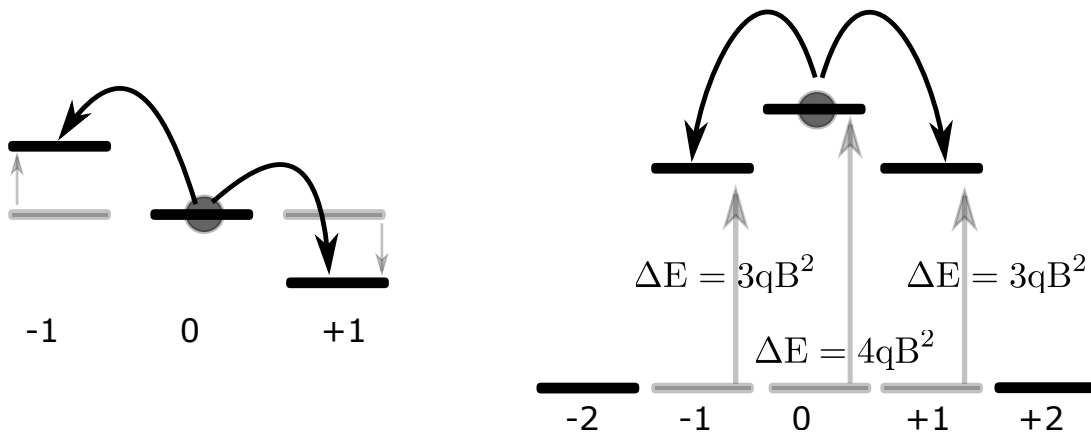


Figure 6: **Energy shift of the hyperfine levels due to the magnetic field. Left:** The linear Zeeman effect shifts the level according to $\Delta E = m_F p B$ with $p \approx 700 \text{ kHz/G}$. **Right:** Second order Zeeman shift for the $F = 2$ manifold. The $m_F = 0$ state has an effective detuning of $\Delta E_B = qB^2$ with $q \approx 72 \frac{\text{Hz}}{\text{G}^2}$ with respect to the $m_F = \pm 1$ states. As the $m_F = \pm 2$ have no second order Zeeman shift, Spin-changing collisions processes, which directly couple to $m_F = \pm 2$ are tuned out of resonance and we can treat it as an effective spin-1 system, as discussed in chapter 2.

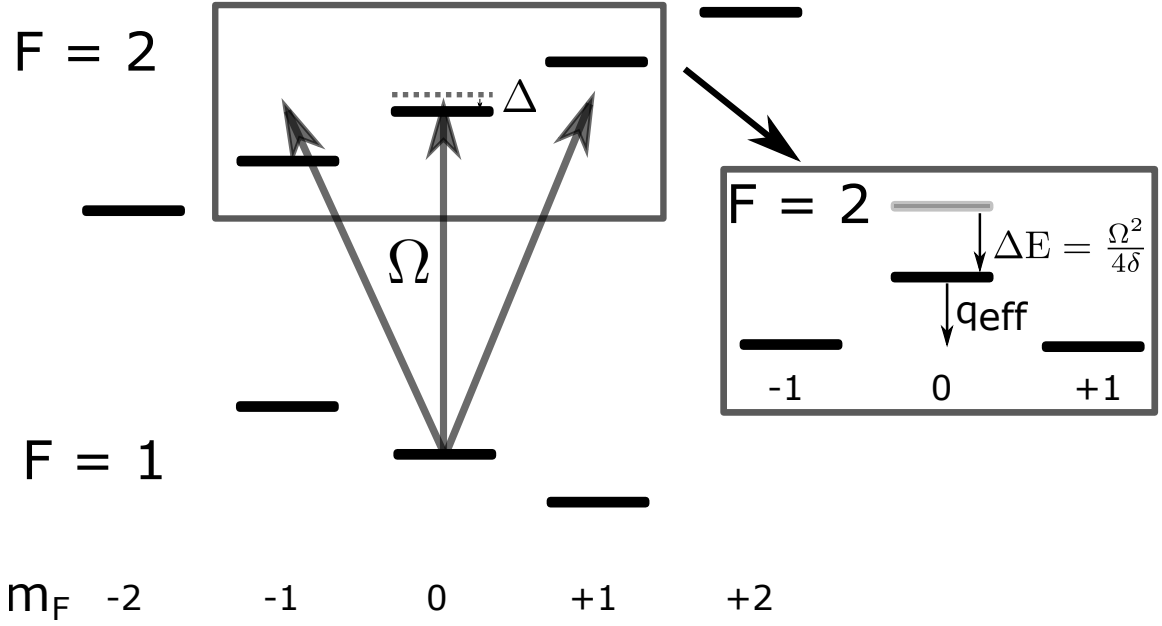


Figure 7: Hyperfine groundstate manifold of ^{87}Rb with energy splitting due to the linear Zeeman effect. The microwave dressing has a detuning $\Delta \gg \Omega$ relative to the $|1, 0\rangle \rightarrow |2, 0\rangle$ transition and shifts the $m_F = 0$ state by $\Delta E = \Omega^2/4\delta$. With this the parameter q_{eff} can be changed just by changing the detuning of the microwave radiation while the Rabi frequency is kept fixed. However, all other shifts coming from coupling to $m_F = \pm 1$ can be neglected as they are far too off-resonant.

state-selective off-resonant microwave dressing [18] between $F = 1$ and $F = 2$. For this the atoms are subjected to microwave magnetic fields with Rabi frequency Ω and detuning Δ from the atomic resonance. The effect can be described by the Hamiltonian [19]

$$\mathcal{H} = \frac{1}{2}(\Omega\sigma_x - \Delta\sigma_z), \quad (40)$$

where σ_i are the spin-1/2 Pauli matrices [20]. This Hamiltonian can be diagonalized and in the eigenbasis, the so-called dressed states, the energy shift is given by:

$$\Delta E_{\text{MW}} = -\frac{\delta}{2} + \sqrt{\Omega^2 + \delta^2} \stackrel{\Omega \ll \delta}{\approx} \frac{\Omega^2}{4\delta} \quad (41)$$

Applying the radiation close to the resonance to the $|F = 1, m_F = 0\rangle \rightarrow |2, 0\rangle$ transition, we can shift the pump mode and the dressing can effectively be seen as a magnetic field shift, resulting in:

$$q_{\text{eff}} = \Delta E_B + \frac{\Omega^2}{4\delta} \quad (42)$$

3.3.3 Spatial Gradients

Magnetic field gradients can lead to spin domains even in the ground state of a spinor BEC [21]. We want to study the size of spin structure emerging after introducing an instability. Therefore, we want to have magnetic field gradients which are small compared to the SCC interaction strength.

For cancelling out magnetic field gradients, we drive a small coil with 5 windings as close as possible to the experimental chamber, with a laser diode current driver. The residual magnetic field gradient is measured with a Ramsey sequence on the $|F = 1, m_F = 1\rangle \rightarrow |1, -1\rangle$ transition with 100 ms interrogation time, by means of microwave coupling and intermediate coherent state swapping between $|2, 0\rangle$ and $|1, -1\rangle$ (Fig. 8 a). We can only give an upper bound on the gradient, as the measurement is not reliably working for small gradients. A possible reason for this is spin dynamics happening in the waiting time, as this cannot be fully excluded at 0.8825 G. Fig. 8 shows the result of this measurement for a small gradient, where the fitting procedure is still working. Although there should be no mean field shift between the two levels the wavelength seems to change with position. A possible explanation is a small gradient of the gradient, which gets visible compensating the real gradient and both becoming on the same order. This setting sets the limits of the magnetic field gradient, but it can be compensated better. When we write the magnetic field as $B = B_0 + B'x + B''x^2$, we can make a fit to imbalance profile of the form

$$I(x) = A \sin(2\pi t_{\text{int}}(pB'x + pB''x^2) + \phi)$$

with $t_{\text{int}} = 100$ ms the interrogation time. The fit results in:

$$B' < 9 \frac{\mu\text{G}}{120 \mu\text{m}} \quad (43)$$

$$B' < 2.5 \frac{\mu\text{G}}{(120 \mu\text{m})^2} \quad (44)$$

The energy mismatch q_{eff} is adjusted with microwave dressing. Inhomogeneous microwave radiation can generate a further gradient in the effective detuning of the SCC q_{eff} . For determining the strength of the gradient we evaluate the spatial profile after 100 ms of resonant Rabi flopping. We find a gradient of 0.037 Hz/ μm which amounts to 0.1%.

As a result we can neglect the dressing gradient as it is strongly suppressed. In the case of the magnetic field we have to take a closer look on the dynamics as the energy scale for the magnetic field is dominantly given by the linear Zeeman shift. This results in a shift on the order of Hz and its influence is yet not understood and under investigation.

3.4 Experimental Sequence

After a first stage of evaporative cooling in a magnetic TOP trap [22] in the $|1, -1\rangle$ - state, the atoms are loaded in a crossed optical dipole trap. After a second stage of evaporative cooling below the transition temperature [23] by reducing the laser power adiabatically, we are left with around 25000 Bose condensed atoms. The second beam of the crossed dipole trap is slowly switched off and the atoms are released in the elongated trap described in

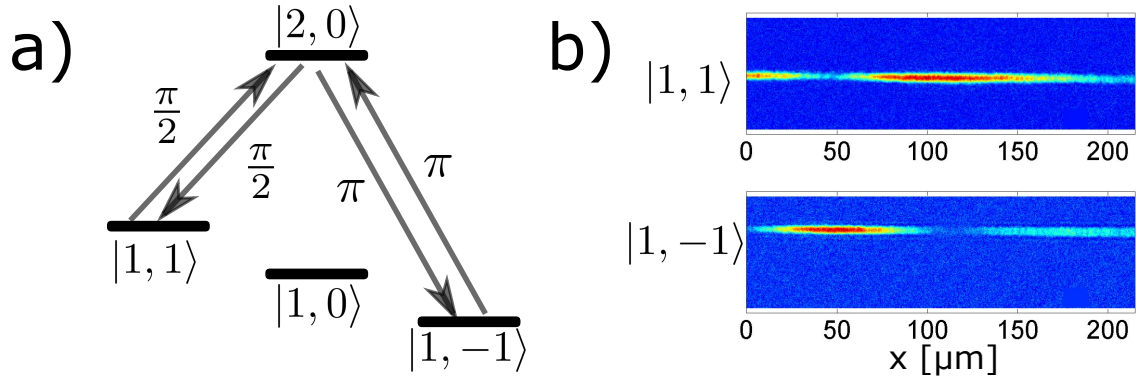


Figure 8: a) Ramsey sequence: Starting in $|1, 1\rangle$ half of the population is transferred into $|2, 0\rangle$. To avoid a mean-field shifted signal the atoms are transferred to $|1, -1\rangle$ and then hold for 100 ms. In the reverse way the phase evolution is read out. b) Spatial profile of $|1, 1\rangle$ and $|1, -1\rangle$ after phase evolution and read out. A sinus with varying spatial frequency according to a slowly varying magnetic field gradient is fitted to the population imbalance. As a result, the gradient for this setting is smaller than $9 \mu\text{G}/120 \mu\text{m}$.

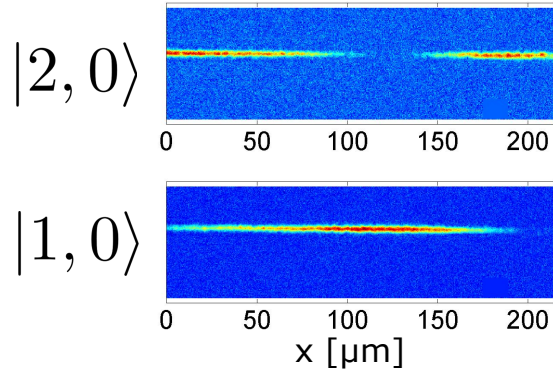


Figure 9: Population in $|1, 0\rangle$ and $|2, 0\rangle$ after a 100 ms resonant Rabi pulse coupling the two levels. The variation with x is sinusoidal, indicating a linear power gradient along x . For a Rabi frequency $\Omega = 4.04 \text{ kHz}$ the relative error from edge to edge is 0.1% and is therefore strongly suppressed.

section 3.1.

With a microwave π - pulse the atoms are transferred to the $|2, 0\rangle$ - state and spurious atoms in other states are removed from the trap by a Stern-Gerlach magnetic field gradient. To initiate the dynamics the microwave dressing is switched to the final value of q_{eff} at a magnetic field of 0.8825 G. After an evolution time of t_{evo} the atoms are either directly imaged as described in section 3.2 or the spin is rotated by a $\pi/2$ rf-rotation before imaging.

After 50 experimental realizations the magnetic field is controlled by doing Ramsey spectroscopy and readjusted if necessary to avoid drifts of the magnetic field on long time scales.

3.5 Experimental Observables for Detecting Spin Structures

The excitations predicted by Bogoliubov theory are excitations of the spin lying in the x- and y- plane. As already discussed, this spin directions can be mapped onto the population imbalance. After the rotation all five components of the $F = 2$ manifold are occupied. Thus we have to calculate the spatial spin profile as the expectation value of the real spin-2 F_z matrix, given as:

$$\langle F_z \rangle \propto 2N_{+2} + N_{+1} - N_{-1} - 2N_{-2} \quad (45)$$

For analysis of spin excitations with a wavelength much smaller than the cloud size, the spin profile is normalized to the local total atomnumber per pixel. Furthermore the mean spin offset per shot is subtracted and three pixels are binned to suppress effects coming from the imaging resolution of $1 \mu\text{m}$.

The theorem of Wiener and Khinchin [24, 25] states that the Fourier transformation, or the power spectrum, and the spatial correlation function are connected by a Fourier transformation. So, in principal both should give the same information about the system. A peak in the Fourier spectra in the regime of k_{mu} can be much better extracted as the period of the correlation function. In the regime where only small k are unstable, however, the structure size cannot be reconstructed from the Fourier spectra and the correlation function gives easily access by the first minimum as described later.

The Fourier transform is calculated with a discrete Fourier transformation, where the Fourier component is given as the overlap of the spin profile with the phase factor $e^{-i2\pi kx}$ calculated with a discrete sum. The spatial frequencies are given as $k = 1/\lambda$, where λ is the wavelength of the spatial excitations, missing the 2π factor of a real momentum, thus the spatial frequency can directly be converted into a structure size.

Structures appearing nearly periodically can be identified by calculating correlation functions. The correlation function of an observable A is calculated as follows:

$$G(\Delta x) = \sum_x A(x) A(x + \Delta x) \quad (46)$$

This process gives rise to a better signal-to-noise ratio as the Fourier transform, because every point is an average over the whole profile. With this inherent averaging process technical fluctuations are suppressed [26].

Intuitively, for a fixed distance Δx , it is given as the overlap of the profile with the same

profile shifted by Δx . As the mean is subtracted, $G(0)$ gives directly the variance of the spin fluctuations in the single shot [27].

For both methods the calculation is done for every single realization and then the mean is taken over at least 30 realizations with the same setting of parameters. The stability of emerging structures is investigated by comparing single realizations.

4 Spin Exchange Dynamics and Growth Rate

In this chapter, we examine spin changing collision dynamics in the F_z -direction. A typical evolution of the side mode population is shown. Furthermore, we show how the mode population and the Fourier transform of the spatial profile are connected. With this we can determine the growth rates for different spatial frequencies and compare them to Bogoliubov theory.

4.1 Time Evolution

First, we determine the side mode population as a function of time while population transfer due to spin changing collisions is tuned into resonance, i.e. the system is unstable. For this we prepare around 22000 atoms in the $|2, 0\rangle$ state as described in chapter 3. After switching on the microwave dressing the side modes get populated. In Fig. 10 the fractional population is shown. The points are the mean value of ≈ 100 experimental realizations and the errorbars are given by one standard deviation of the mean. We see a fast growth of the population up to 110 ms. After that it oscillates back into the $m_F = 0$ state which is a signature of the coherence of the process [28].

We see a dependence of the growth rate on the detuning q_{eff} as expected by Bogoliubov theory. Thus we look at the growth of the momenta close to the most unstable Bogoliubov mode in the Fourier spectrum. Its behavior is expected to be exponential with the growth rate given by twice the imaginary part of the eigenenergy.

4.2 Calibrating the Fourier Transform

The Wiener-Khinchin theorem helps us finding a relation between the Fourier transform of the spatial profile and the population of the momentum modes. As the power spectrum is given by the squared Fourier transform, the population is directly proportional to the squared Fourier amplitude. So we just have to sum up the squared Fourier amplitudes and can plot them versus the side mode population. A linear fit gives the proportionality constant.

We post process the spatial profile in the same way as the spin. We fit a parabolic function and subtract it to get rid of the spatial profile have a profile centred around zero [26]. The squared mean Fourier transform is plotted versus the spatial frequency $k = 1/\lambda$ in Fig. 11 (left panel). The dashed line is taken after negligible evolution time, i.e. it shows the initial condition. The black dashed line is taken after 48 ms of evolution time. A substantial growth of the population can be directly seen. The grey line shows the unstable momentum sector predicted by Bogoliubov theory. This is in qualitative agreement. A quantitative comparison will be given in sect. 5.2.

Summing up over all momentum modes we get the total population. The mean side mode population is plotted versus the summed Fourier amplitudes in Fig. 11 (right panel). It is consistent with the expected linear behaviour. A linear fit gives (3600 ± 800) atoms/amplitude unit for the $m_F = +1$ state. The fit gives a small negative offset, which is due to the background noise level of the FFT giving a signal although there are no atoms scattered into the side modes.

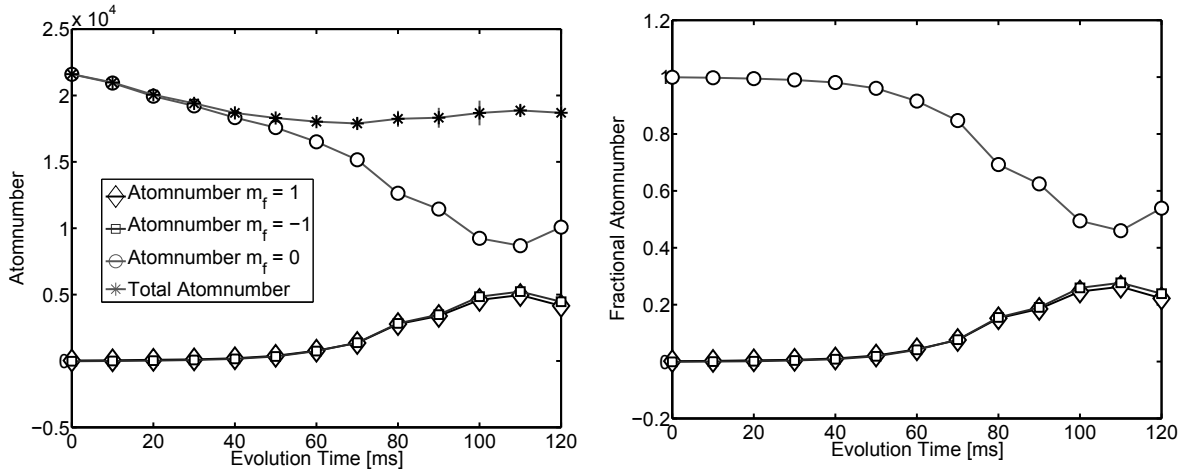


Figure 10: **Total side mode population versus evolution time.** Around 22000 atoms are prepared in the $|2,0\rangle$ state and spin-changing collisions are tuned into resonance for $q_{\text{eff}} = 2\pi \times -5$ Hz. In the right panel the total atom number is plotted and in the left panel the fractional atom number normalized to the total atom number is shown. One can see a substantial growth of the population up to 100 ms. The oscillation back into the pump mode after ~ 110 ms demonstrates the coherence of the scattering process.

We now can convert the Fourier transform into occupation numbers for the F_z imaging. After the rotation this is not possible as in this case we are detecting spin excitations and have no reference for calibrating the amplitudes. Though, we still know that the squared amplitudes are proportional to an occupation number.

4.3 Measuring the Growth Rate

With the calibration of the Fourier amplitudes it is possible to measure the growth rate of the occupation of the spatial frequencies and compare it with Bogoliubov theory. The occupation in one side mode is predicted to be given by [7]

$$n_{k,i} = \langle b_{k,i}^\dagger b_{k,i} \rangle = \sinh^2(\gamma_k t) \quad (47)$$

with $\gamma_k = \text{Im}(\omega_{k,i})$ and $i = \pm 1$. In Fig. 12 a) we plot the time evolution of the squared Fourier amplitude. We extract the growth rate by fitting the slope a_{fit} after 30 ms of evolution time. The constant population of ~ 10 is due to a constant noise background. From the slope we get the growth rate

$$\gamma_k = \frac{a_{\text{fit}}}{2} \quad (48)$$

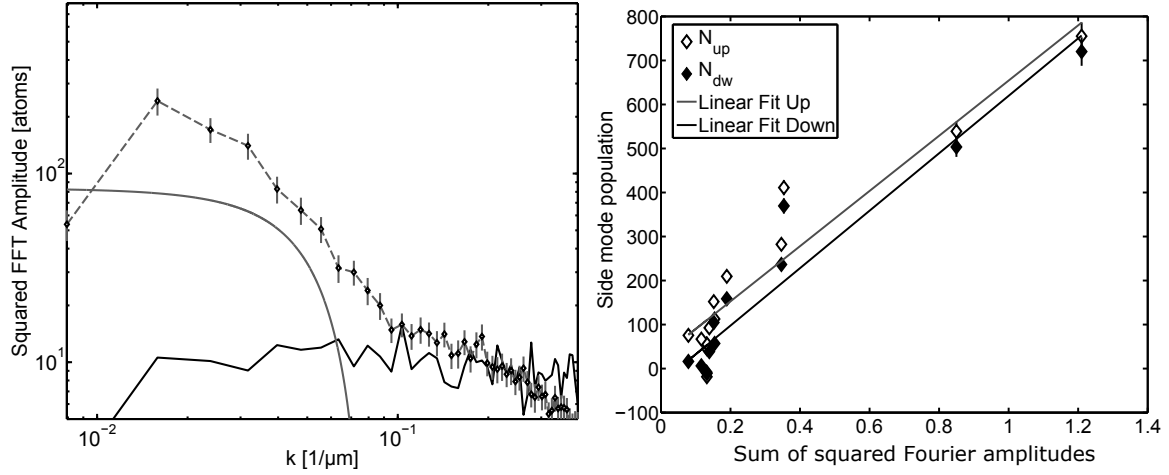


Figure 11: **Typical Fourier spectrum and calibration of the population** In the left panel a typical Fourier spectrum of the $|1, -1\rangle$ state after 48 ms of spin changing collisions at $q_{\text{eff}} = 2\pi \times -12$ Hz (grey dashed line) is shown. Here the squared absolute values are plotted versus the spatial frequency $k = 1/\lambda$. The black solid line shows the initial state. The grey line shows the unstable section of the Bogoliubov dispersion relation. In the right panel the side mode population of $m_F = \pm 1$ (black, gray diamonds) is plotted versus the squared Fourier amplitudes summed over all spatial frequencies. A linear fit gives the calibration factor from FFT amplitude to occupation number. For $m_F = +1$ we get (3600 ± 800) atoms/amplitude unit and for $m_F = -1$ we get (3590 ± 830) atoms/amplitude unit.

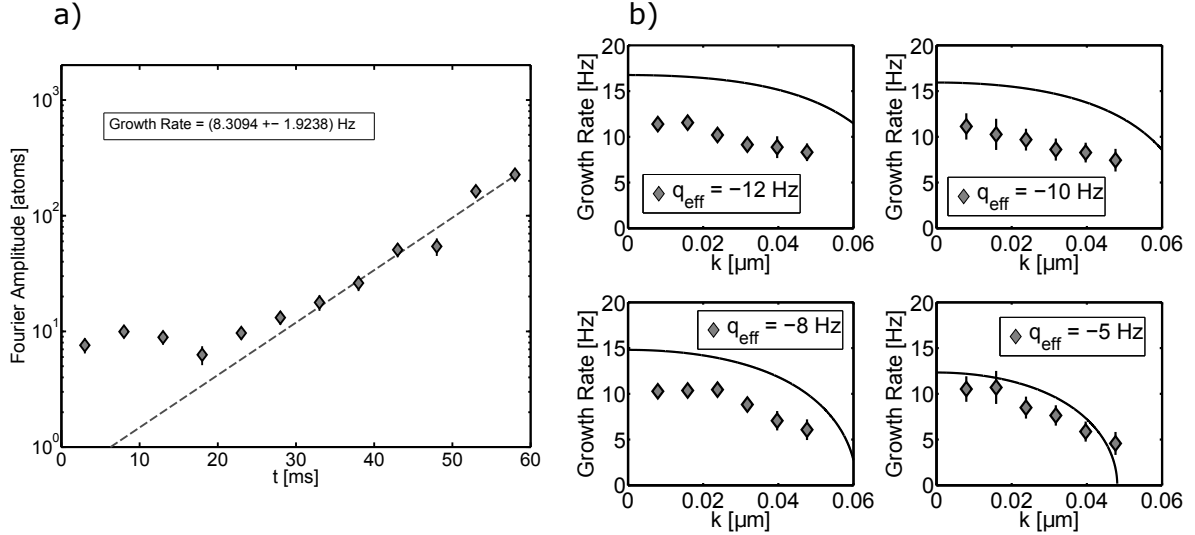


Figure 12: **Growth rate measurement** In a) we plot the Fourier amplitudes converted into occupation numbers versus the evolution time exemplarily for $q_{\text{eff}} = 2\pi \times -12$ Hz and $k = 0.05 \mu\text{m}^{-1}$. We fit the slope of the exponential increase after 30 ms of evolution time and extract the growth rate (main text). The growth rate is plotted (b) for four values of q_{eff} versus the spatial frequency k . The growth rate predicted by Bogoliubov theory (black line) is plotted for $nc_1 = 2\pi \times 17.7$ Hz. We see smaller growth rates than theoretically expected.

The $1/2$ comes from the squared hyperbolic sine in eq. 47. The growth rate extracted for different spatial frequencies in the unstable regime are plotted in Fig. 12 b). The theoretical prediction (black solid line) is plotted for

$$\omega_{k,i} = \sqrt{(\epsilon_k + q_{\text{eff}})(\epsilon_k + q_{\text{eff}} + 2nc_1)}$$

with $nc_1 = 2\pi \times 17.7$ Hz, as determined in chapter 5.

For $q_{\text{eff}} = 2\pi \times -5$ Hz the measured growth rate coincides with the theoretical expectation. However, for $q_{\text{eff}} < 2\pi \times -5$ Hz the experimentally determined growth rates are smaller than predicted. The deviations will be further investigated by comparing the experimental data to simulations solving the coupled Gross-Pitaevski equations in a harmonic trap using the truncated Wigner approximation. With this we can evaluate, whether these deviations are due to the spatial confinement not included in our Bogoliubov theory up to now.

5 Structure Formation in a Spin-1 BEC

In the first chapter, we introduced methods to analyse structure formation while evolving a spin-1 BEC under an instability. In general, these predictions are only true for very short evolution times, i.e. for a small occupation of the unstable modes. Later the Bogoliubov approximation made in the derivation should break down due to the large occupation numbers in the side modes. Thus, we first compare the experimental results for short times with Bogoliubov theory. As the theory is done in a homogeneous system without a trap we identify differences between experiment and theory. For longer times, we see a shifting of the most dominant Fourier component. This can be explained by shifts of the interaction constant nc_1 due to depletion of the pump mode. However, the structure sizes are well described by our initial theory with changed interaction.

5.1 Short Time Evolution of the Fourier Spectra

Linearisation of the equation of motion around a mean field ground state is only possible as long as the population of the non-condensed modes is negligible. Thus, we have to go into an experimental regime where the population of the $m_F = \pm 1$ components is small compared to the $m_F = 0$ component. Without spin-rotation this regime is close to the detection limit and the signal-to-noise ratio is therefore very bad. Hence, we rotate the spin after the evolution time and evaluate the transversal spin. Here, we find a much better signal-to-noise ratio and the structure size can be determined even for short times.

For a qualitative comparison of experiment and theory we want to make use of the Fourier spectra. As we will see later, the autocorrelation function is better suited for a quantitative comparison. In the preceding chapter we showed that the squared amplitudes of the Fourier spectra are proportional to the occupation number of the side modes. So they should in this case give the occupation number of the spin modes. In Fig. 13 an exemplary Fourier spectrum is shown. The black dashed line is the Fourier spectrum after negligible evolution time and represents the initial state. It defines the noise background on top of which we are looking for structure. The grey diamonds are the experimental data after 55 ms of evolution time and for $q_{\text{eff}} = 2\pi \times -22$ Hz and the errorbars are given by the statistical error of the mean. The black solid line gives the unstable momentum region predicted by Bogoliubov theory for $nc_1 = 2\pi \times 18$ Hz. We see a good qualitative agreement especially in the cut off frequency beyond which no exponential growth due to unstable modes is expected. We see that in this regime of q_{eff} a broad range of modes is able to grow with nearly the same instability rate. The stable regime can be well identified by comparing to the initial state.

5.1.1 What Are Short Times?

For extraction of the structure sizes we want to maximise the signal-to-noise ratio. For this, we will have a look at the time evolution of the Fourier spectrum of the transversal spin profile. As long as the qualitative form is not changing but the amplitudes in the unstable region are just growing by an equal amount, we can use the time as comparison for the short time theory. After 40 ms of evolution time we can definitely speak of a signal showing

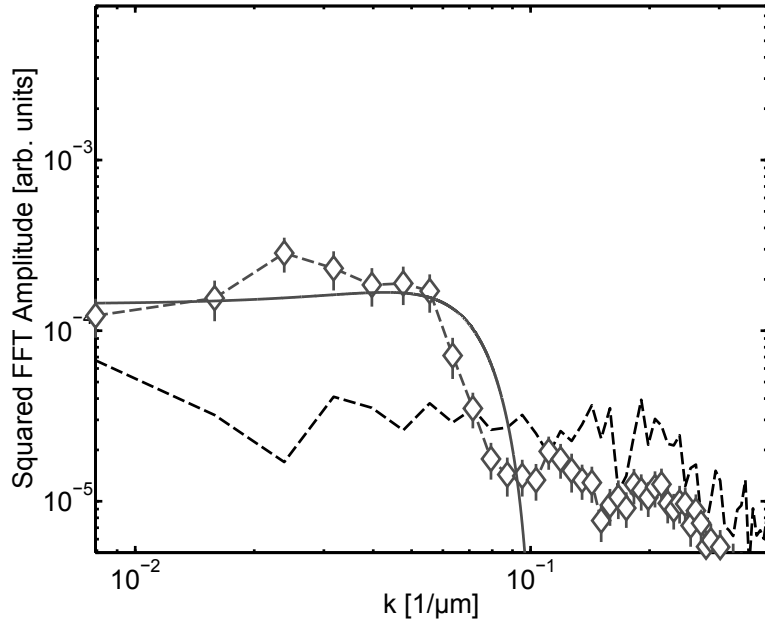


Figure 13: **Exemplary plot of the squared Fourier amplitudes** of the transversal spin profile and q_{eff} is set to $2\pi \times -22$ Hz. The dashed grey line represents the initial condition. The diamonds are the experimental results after 55 ms and the errorbars are given by the statistical error of the mean. The data shows qualitative agreement with the region of unstable modes for $nc_1 = 2\pi \times 18$ Hz, plotted as grey solid line.

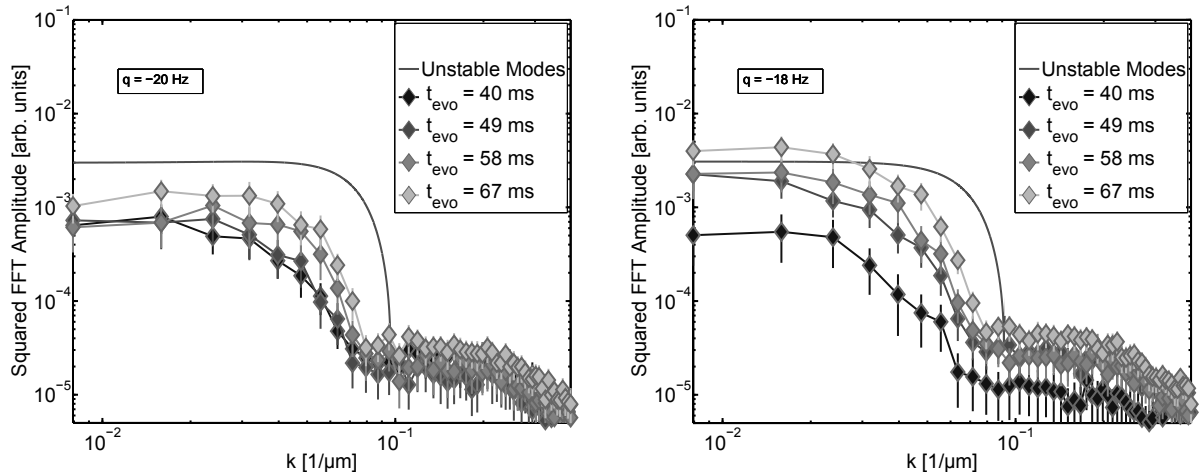


Figure 14: **Short time evolution of transversal spin Fourier spectra.** We plot squared FFT amplitudes against the spatial frequency k in a double-logarithmic plot and see growing population with rising evolution time for $q_{\text{eff}} = 2\pi \times -20$ Hz (left panel) and $q_{\text{eff}} = 2\pi \times -18$ Hz (right panel). The region of unstable modes is plotted for $nc_1 = 2\pi \times 18$ Hz (grey solid line). After 60 ms the qualitative shape changes and thus we use only times ≤ 60 ms for short time comparison.

up in the spectra. In Fig. 14 the spectra are shown for 4 different evolution times and two different detuning. We see that the population is growing from 40 up to 60 ms and the region of unstable modes does not change. However, after 60 ms we see first indications of a changing Fourier spectra which will be discussed later. This is accompanied by more than 10% side mode population as we can see in Fig. 10. For this population the Bogoliubov approximation should slowly break down. Thus we can state, evolution times up to 60 ms can be used to compare the experimental data to the Bogoliubov theory expanding the Hamiltonian around the polar state.

5.2 The Cut-Off Frequency

The comparison with the least assumptions we have to make is to determine the cut off frequency, i.e. the smallest spatial frequency which does not get exponentially populated. This frequency is easily calculated from the dispersion relation and is depending on q_{eff} .

The dispersion relation for the spin fluctuations in the x-y-plane is given by

$$\omega_k^2 = (\epsilon_k + q_{\text{eff}})(\epsilon_k + q_{\text{eff}} + 2nc_1). \quad (49)$$

Setting equation (49) to zero we can find the boundaries of the unstable region. For $0 > q_{\text{eff}} > -2nc_1$ all modes up to a cut off k_{co} are unstable. So the root we are looking for

is given by $(\epsilon_k + q_{\text{eff}}) = 0$ and the cut off frequency k_{co} is

$$k_{co} = \sqrt{-\frac{2M}{h}q_{\text{eff}}}. \quad (50)$$

In Fig. 15 the q value that we can associate with the cut off frequency by equation (50) is plotted against the detuning adjusted experimentally. The homogeneous theory predicts a line with slope 1 which is shown as grey straight line. The experimental data is shown as grey diamonds. In the inset the determination process is shown. The squared FFT amplitudes are plotted semi-logarithmically against the spatial frequency k . The cut off frequency is roughly guessed and for the next view points with larger k a mean value is calculated giving the niveau of the stable population. The crossing between experimental data and mean gives the cut off frequency.

To quantify the deviations we make a linear fit resulting in:

$$q_{co} = (0.9 \pm 0.10) q_{\text{eff}} + (0.7 \pm 0.4) \text{ Hz} \quad (51)$$

Here we see the first indications for deviations from the homogeneous theory. The slope is within the errorbars consistent with 1. We find an offset which is not predicted by the homogeneous Bogoliubov theory. However, we cannot fully explain it up to now and it is within 2σ consistent with zero. Thus, we will not take it into account in the following discussion.

5.3 Extracting Structure Sizes

For comparing the theoretical predictions with the experimental data, we want to have a reproducible and robust method to extract the dominant structure size. In the regime $-nc_1 \leq q_{\text{eff}} \leq 0$ the most unstable mode is given by $k = 0$ followed by many modes with nearly equal instability rate. This broad window of modes leads to a flat occupation up to the cut off frequency. Thus the structure size of the spatial profile cannot be well extracted. In this part, we want to introduce the correlation function as a robust tool to identify the structure size.

When we want to extract the structure size of a spin profile with structures with slightly changing sizes and nearly periodic distance the Fourier transform is not the optimal method. First of all, the limited window size gives only few periods of the signal. Further, the changing size washes out the expected peak in the Fourier transform. A better result can be obtained by using the spatial correlation function introduced in chapter 3. Intuitively, the correlation function is positive (negative) for (anti)correlated signals. Fully uncorrelated signals give a zero correlation function. Here, we use the auto correlation of the rotated spin profile. For zero lag the correlation is maximal and the first minimum gives the mean distance of two neighbouring structures. We extract the structure size ξ as

$$\xi = 2 \Delta x_{\text{min}}. \quad (52)$$

We checked the validity of this method by comparing to the peak in the Fourier spectra.

In Fig. 16 different experimental realizations of the auto-correlation function of the spin profile are shown. In the regime $-2nc_1 \leq q_{\text{eff}} \leq -nc_1$ (left panel) the most unstable

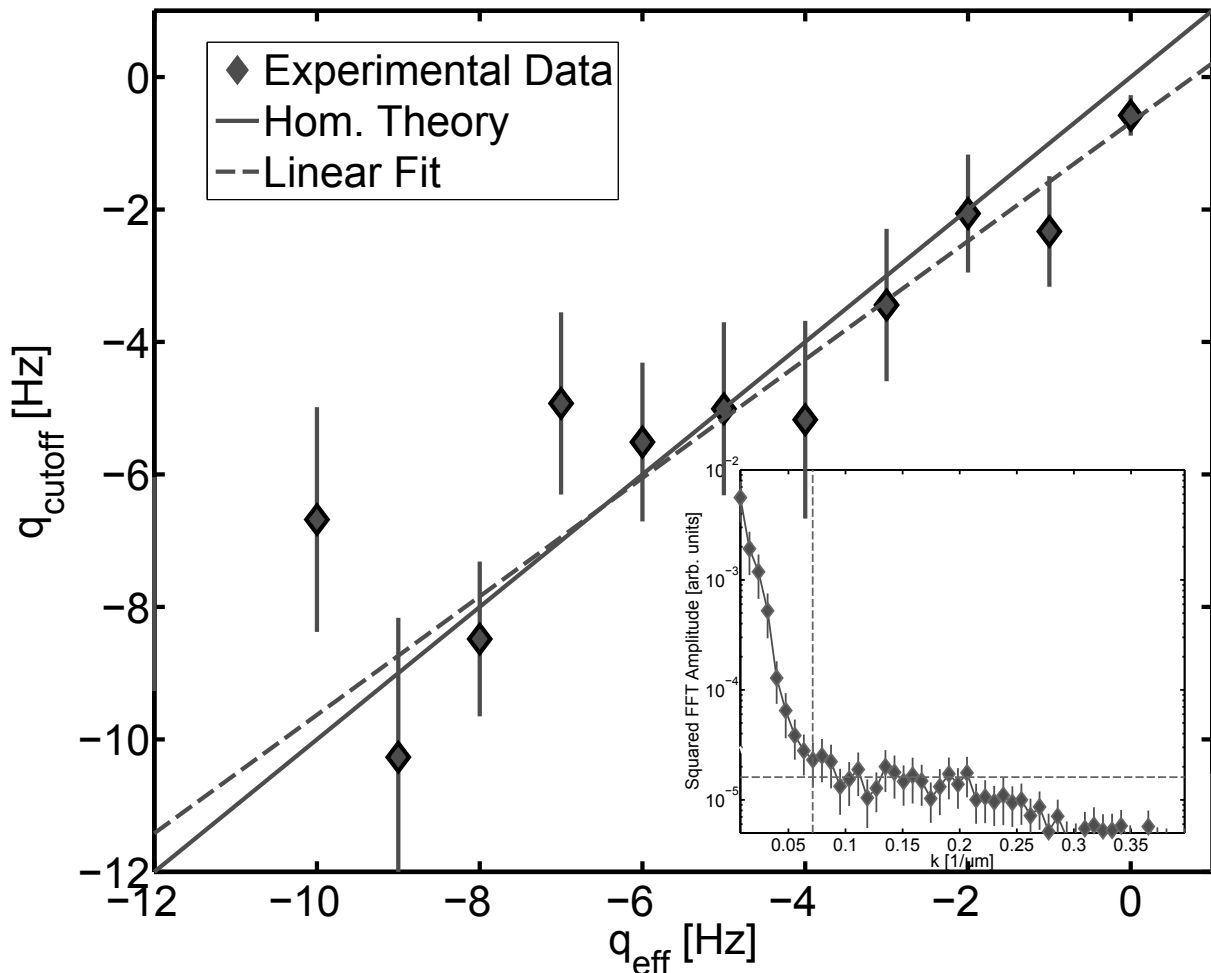


Figure 15: **Cut-off frequency in units of the detuning q_{eff} plotted against the experimental adjusted detuning.** The grey diamonds show the experimental results and the errorbar is given by the read-off accuracy. The cut-off frequency is determined after 60 ms of evolution time and rf-rotation. An exemplary Fourier spectrum is shown in the inset. The intersection between the amplitudes and a mean level is taken as the cut-off and the Fourier spectra are obtained as previously described. The expectation of the homogeneous theory is plotted as grey solid line. We find a slope which is within the errorbars consistent with 1.

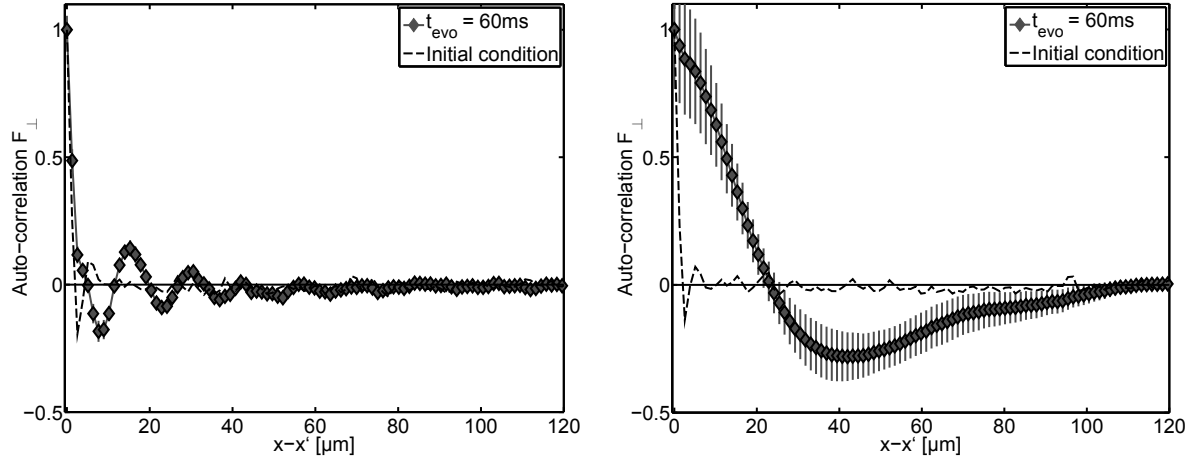


Figure 16: **Auto correlation function of rotated spin profile** Here the auto correlation is plotted against the distance $x - x'$ for $q_{\text{eff}} = 2\pi \times -26\text{ Hz}$ (left) and $q_{\text{eff}} = 2\pi \times -6\text{ Hz}$ (right) for evolution time 60 ms (grey diamonds). In the left panel q_{eff} is in the regime where the most unstable mode is not equal to zero and short range correlation can be seen in more than 3 periodic oscillations. On the right side we are in a regime where theoretically $k = 0$ is most unstable. However, the structure size is bounded from above by the window size of the camera image ($120\ \mu\text{m}$). The error bars are given by the error of the mean and the initial condition is plotted as grey dashed line.

mode is predicted to be non zero, i.e. one would expect structures on the order of $1/k_{mu}$ and oscillations in the correlation function, what clearly can be seen. The damping of the oscillation is due to not perfect regularly patterns as well as the biased calculation of the correlation function. This algorithm always normalises to the length of the full sample which causes damping in system without periodic boundary conditions.

The regime $-nc_1 \leq q_{\text{eff}} \leq 0$ should yield deviation from the homogeneous Bogoliubov theory. Theoretically the $k = 0$ mode should be most unstable but experimentally we are limited by the lowest trap levels. Comparing to Fig. 13 we see in this regime a broad plateau of grown modes, which makes it impossible to extract a mean structure size. However, the correlation function in Fig. 16 shows a clear minimum around $40 \mu\text{m}$ and we are able to extract a structure size out of it.

With the correlation function as a tool to extract the dominating structure size we are now able to make quantitative comparisons between experiment and theory.

5.4 Comparing Short Times to Bogoliubov Theory

With the dispersion relation deduced in chapter 2 we can make predictions about the unstable spatial frequencies growing for a certain q_{eff} . We want to compare this to the experimental results by extracting the structure size as explained before.

Let us first have a look at the dispersion relation

$$\omega_k = \sqrt{(\epsilon_k + q_{\text{eff}})(\epsilon_k + q_{\text{eff}} + 2nc_1)}. \quad (53)$$

We find the most unstable mode by looking for the minimum of ω_k^2 as

$$k_{mu} = \sqrt{-\frac{2M}{h}(q_{\text{eff}} + nc_1)} \quad (54)$$

for $q_{\text{eff}} < -nc_1$ and 0 for $-nc_1 < q_{\text{eff}} < 0$.

We extract the structure size as described in the previous section by fitting a parabolic function around the minimum as shown in Fig. 17. Plotting the data in two different ways allows us to have a closer look in two different regimes. The structure size directly determined from the correlation function shows the behaviour for q_{eff} going to zero. In the regime $-nc_1 \leq q_{\text{eff}} \leq 0$, $k = 0$ is the most unstable mode in the homogeneous theory and the size of the window of unstable modes is also going to zero. Therefore the structure size should grow.

By calculating an associated k^2 from the structure size we can closer investigate the transition at $q_{\text{eff}} = -nc_1$ and also the further evolution for smaller q_{eff} . The theoretical prediction should be recovered for smaller q_{eff} as there the spectra are dominated by the most unstable mode which is not equal to zero.

First, let us have a look at the squared spatial frequency in the upper part of Fig. 18, where the experimental data is plotted for an evolution time of 60 ms. Up to $2\pi \times -10$ Hz, it stays nearly constant followed by a smooth rising. For $q_{\text{eff}} \leq 2\pi \times -20$ Hz the experimental data follows the prediction by Bogoliubov theory for the most unstable mode (gray dashed line). To find nc_1 we fit the experimental data to equation 54 between $2\pi \times -30$ Hz and

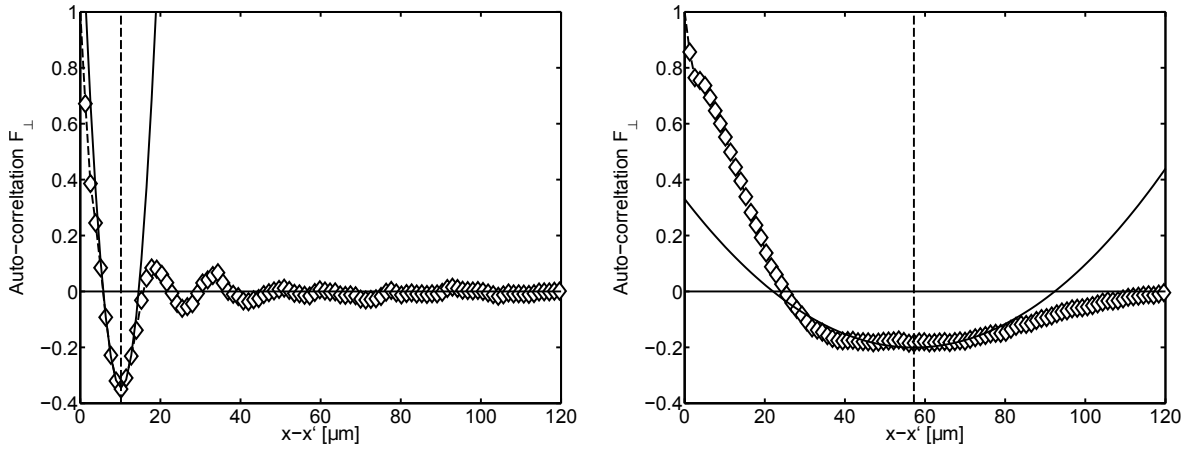


Figure 17: **Extraction of structure size from the correlation function** For the extraction we manually set the upper and the lower bound of fit regions and fit a parabolic function to the correlation function around the minimum. From the fitted minimum we extract the structure size as $\xi = 2 \Delta x_{\min}$. In the left panel, the situation is exemplary shown for $q_{\text{eff}} = 2\pi \times -22$ Hz. For this regime the structure size can be well extracted. In the regime $q_{\text{eff}} > 2\pi \times -10$ Hz, however, the structure size is large, what causes a broad minimum. Additionally the minimum is flattened by the normalization of the correlation function.

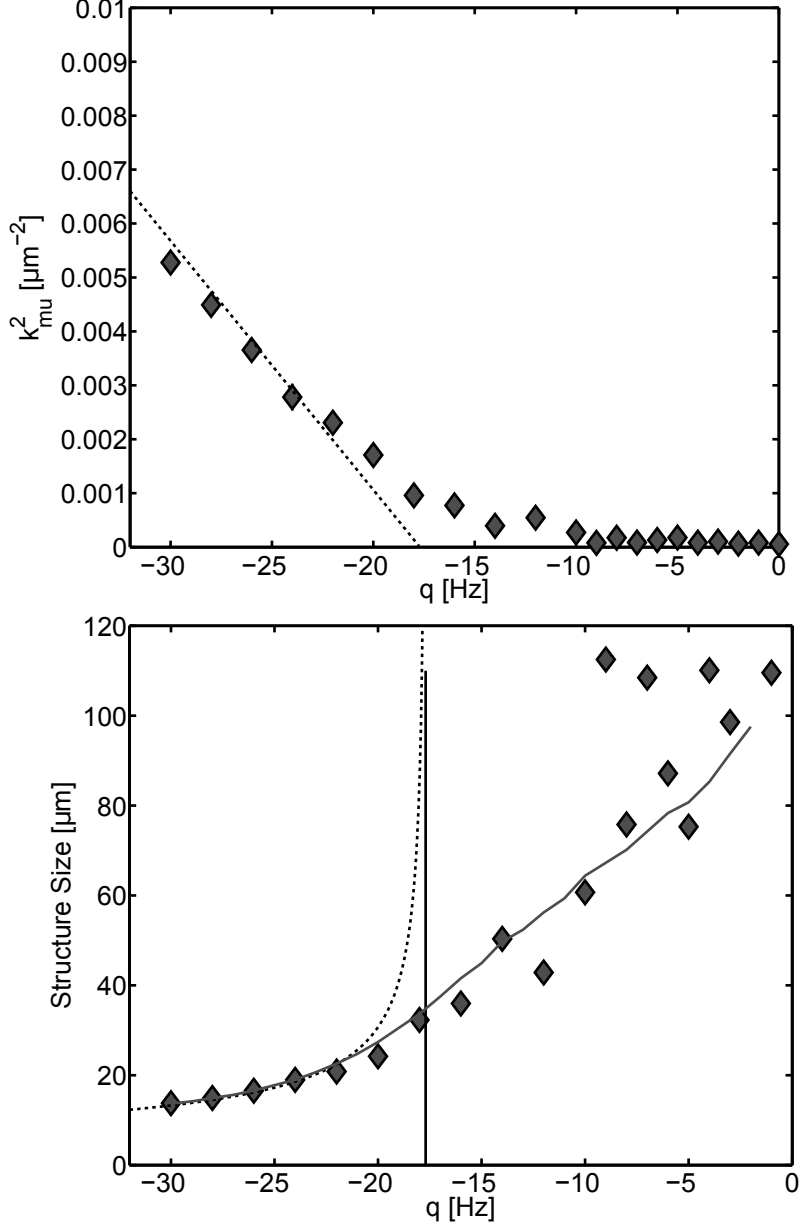


Figure 18: **Comparison of Bogoliubov theory and extracted structure size** We plot the extracted structure size in two ways: The associated k^2 and the structure size. In the upper plot we show k^2 versus q_{eff} and see agreement between theory (black dashed line) and experiment (grey diamonds) for $q_{\text{eff}} < 2\pi \times -23$ Hz. To determine the interaction strength nc_1 we fit in this region the theoretical prediction yielding $nc_1 = 2\pi \times (17.7 \pm 0.9)$ Hz. In the lower plot the structure size is shown. For $q_{\text{eff}} = -nc_1$ the prediction for the most unstable mode diverges. We see, however, finite structure sizes which are limited by the finite window size of $120 \mu\text{m}$. The experimental data is in agreement with a simple theoretical model (grey solid line) obtained by superimposing all unstable trap modes (main text).

$2\pi \times -20$ Hz. From this we find

$$nc_1 = 2\pi \times (17.7 \pm 0.9) \text{ Hz.} \quad (55)$$

For plotting the theoretical data the determined nc_1 is used.

Now let us have a closer look what happens for q_{eff} going to zero. In our situation, having spatial confinement, we have to keep in mind that no real $k = 0$ exists, but we are limited by low lying excitations of the harmonic trap. We can estimate the biggest spatial excitation using the Thomas-Fermi radius. Assuming that the trap is filled by the BEC up to the chemical potential and we look for single particle excitations on top of this effective box potential, the largest excitations should be on the order of 2 times the Thomas-Fermi radius:

$$k_0 = \frac{1}{2r_{\text{TF}}} \approx \frac{1}{240 \mu\text{m}}$$

Further the theoretical line is deduced from the most unstable mode, but also non-zero k -modes are unstable, so we expect finite structure size for finite q_{eff} .

For q_{eff} going to zero the structure size is smoothly saturating at $120 \mu\text{m}$. We find that the structure size is limited just by the size of the window we are evaluating. From the taken image, we cut out $120 \mu\text{m}$ to have the density as homogeneous as possible.

To get a prediction for the finite structure size from Bogoliubov theory, we make a simple estimation: We take the lowest trap levels according to a box potential [29] with the size of twice the Thomas-Fermi radius. They are populated according to the growth rate predicted by the Bogoliubov dispersion relation. After superimposing them with random phases we evaluate the arising pattern in the same manner as the experimental data, i. e. by finding the structure size by means of the correlation function. For this, we take the mean over 1000 realizations, as we want to average over different random phases. Leaving the theory evolution time as a free parameter, we find quantitative agreement especially in the regime from $2\pi \times -30$ Hz to $2\pi \times -10$ Hz. The theoretical evolution time to reconstruct the observed structure size is ~ 125 ms what is approximately twice the experimental evolution time. This does not match with our observation of the growth rates in section 4.3, where we found that the experimental growth rates are in general smaller than theoretical predicted.

5.5 Beyond the Short Time Approximation

In the last section we showed that the predictions made by Bogoliubov theory can be mapped on the experimental data for short evolution times. In general the Bogoliubov approximation is only valid for very short evolution times as we have expanded around the polar state, i. e. no population in the sidemodes. We neglected terms in more than second order in the fluctuations and treated the zero momentum mode of the pump as a complex number. For 80 ms of evolution time, however, more than 30% of the population is in the sidemodes and we expect the approximation to break down. In this section, we want to take a closer look at the further evolution of the Fourier spectra, as well as the structure size.

We have already seen in Fig. 14 that the qualitative form of the Fourier spectra changes even for short times. In Fig. 19 the time evolution of the Fourier spectra up to 140 ms is shown. We see agreement between the Bogoliubov dispersion (black dashed line) and the experimental data for 60 ms (green line). Evolving the system further, the most unstable mode shifts to higher spatial frequencies, i. e. to higher energies. After 120 ms there is no shift any more, what coincides with the maximum of the side mode population in Fig. 10. Furthermore, the population amplitude of the peak is growing until this time. For $k \approx 0.1 \mu m^{-1}$ a second peak is growing after 100 ms. However, the cut-off frequency is not shifting and the peaks are well separated, what excludes a broadening of the unstable mode regime up to this value. This is a first indication for processes not predicted by Bogoliubov theory. Between 120 ms and 140 ms the amplitude of the first peak is going down while the second peak is the dominating after 140 ms.

The cut-off frequency setting the edge of the exponentially growing regime of the first peak seems to stay constant over the whole time evolution. As we have shown, the cut-off frequency is determined solely by the parameter q_{eff} . The most unstable mode, however, is also depending on the interaction strength nc_1 as

$$k_{mu} \propto \sqrt{-(q_{\text{eff}} + nc_1)}. \quad (56)$$

For lower nc_1 the most unstable frequency is shifted to higher energies as the detuning is negative and nc_1 positive. Thus, a dynamically changing nc_1 can qualitatively explain the experimental observed changes.

To compare this intuitive explanation with the experimental results we first have a look at the mean maximum density in the center of the trap. In equation (12) we saw that we can get information about the population in the $m_F = 0$ state after the rotation around F_x . The atom number in the $m_F = 0$ is just a quarter of the initial population. To avoid changing atom numbers due to sloshing of the BEC in the trap, we make a quadratic fit and calculate the linear density over 20 pixel symmetrically around the center. In Fig. 20 b) we see the density in $m_F = 0$ and the total density normalized to the density at 60 ms versus time. Both densities are decreasing as the evolution time rises. For the total density this is due to particle loss due to the excited state manifold $F = 2$. The pump mode is additionally depleted due to the spin changing collision process, where the maximum population transfer happens at 120 ms. For comparison, we look at the most unstable mode versus time for $q_{\text{eff}} = 2\pi \times -22 \text{ Hz}$ as shown in Fig. 19. Setting q_{eff} fix we can calculate the interaction strength from the spatial frequency of the most unstable mode with equation (56). Additionally, we extract the structure size from the correlation function and calculate an associate spatial frequency and with this nc_1 . Looking at Fig. 20 we see that the extracted interaction strength is decreasing with evolution time and both methods give similar results.

Knowing the time evolution of both quantities, we can check how the interaction strength changes with the linear density. For $m_F = 0$ the interaction strength is growing with growing density. For the total density, however, the interaction is changing while the density stays nearly constant in the regime of 0.8 fractional density. We conclude that the shifting of the maximum peak in the Fourier spectra is due to changes of the linear density of the $m_F = 0$ state. The effect is not dominated by the loss effects what can be seen by

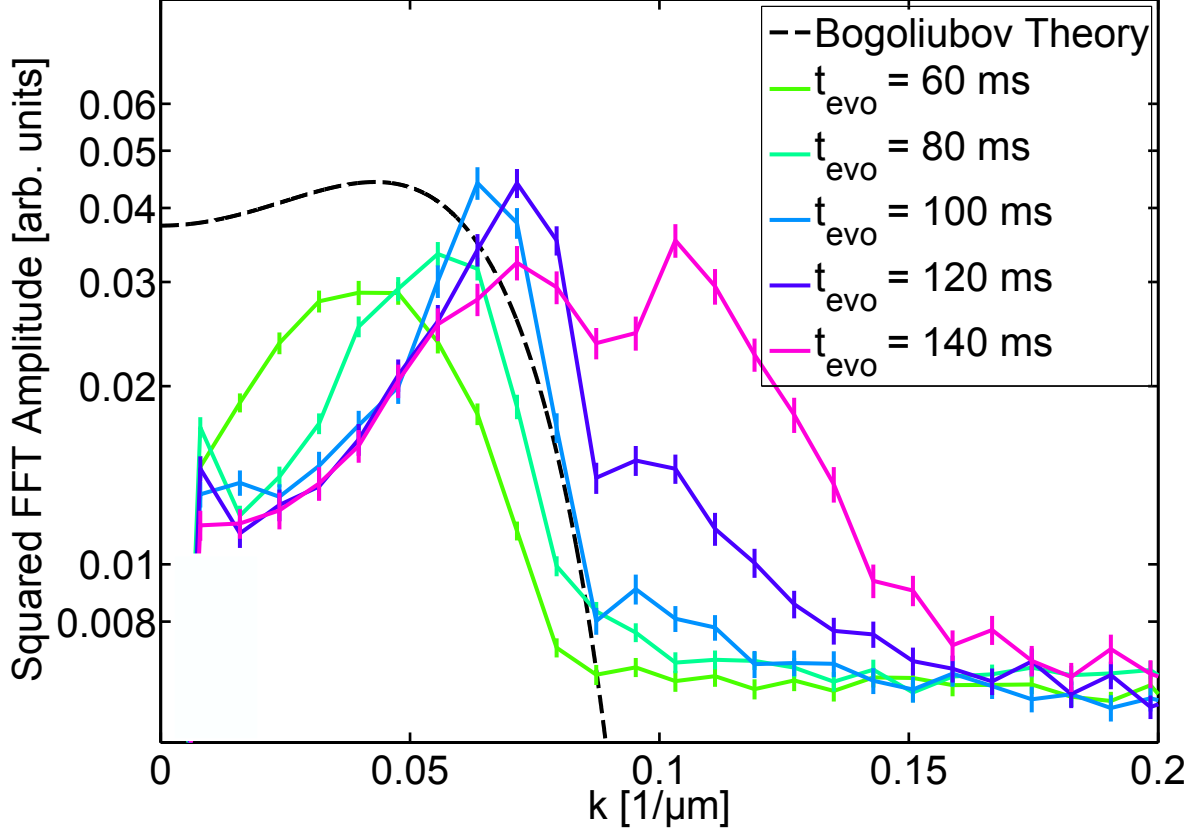


Figure 19: **Fourier spectra for different evolution times** Here we show the squared Fourier amplitudes semi logarithmically versus the spatial frequency k for $q_{\text{eff}} = 2\pi \times -22$ Hz. The regime of unstable momentum modes (black dashed line) is shown for comparison. We see agreement between experiment and theory in the region of unstable modes for an evolution time of 60 ms. Between 60 ms and 120 ms the amplitude of the peak of the most unstable is growing and its position is shifting towards higher spatial frequencies. Separated by the cut-off frequency a second peak is growing after 100 ms. Its position is also shifting in time. A broadening of the unstable momentum region up to $0.15 \mu\text{m}^{-1}$ can be excluded by the minimum between the two peaks. The cut-off frequency seems not to change what leaves the possibility for a changing nc_1 in time.

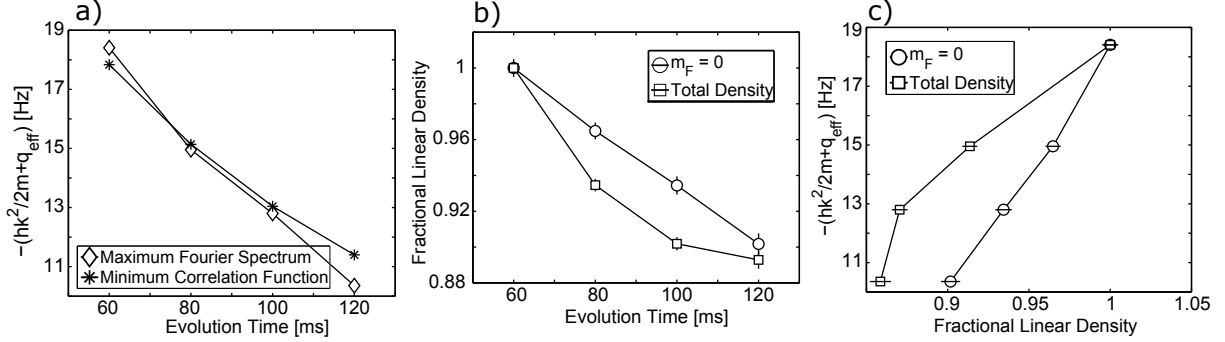


Figure 20: **Dependence of the interaction strength on the linear density** In a) we show the experimental determined interaction strength versus the evolution time. The interaction is extracted from the maximum of the Fourier spectra and from the structure size by evaluating the minimum of the correlation function. With rising evolution time the interaction strength decreases. As the interaction strength is determined by evaluating a single q_{eff} the differences of both extraction methods can be understood from Fig. 18. In b) the linear density is determined by calculating the linear density of 20 pixels symmetrically around the center of the population profile, where the error bar is given by one standard deviation of the mean. We find a decreasing total density, due to losses. The $m_F = 0$ population is affected by the losses but mainly due to the population transfer by the spin-changing collision dynamics. In c) we show the dependence of the interaction strength on the fractional density. As expected, with decreasing density the interaction decreases as well. Thus, we find that the changes of the interaction are dominantly due to population transfer by the SCC process and increased by the particle loss in the system.

looking at the changes of the interaction strength with the total density. The depletion of $m_F = 0$ due to spin-changing collision causes lower density and therefore decreases nc_1 . So we see that the experimental observation fits to the intuitive explanation we gave before.

In 5.4 we have seen that we can describe the experimentally determined structure size with Bogoliubov theory according to an interaction strength of $nc_1 = 2\pi \times 17.7$ Hz over a broad range of q_{eff} . In the last part, however, we showed that the most unstable mode in the Fourier spectra changes with increasing evolution time. We can explain this by effectively changing the interaction strength which is caused by lowering the density of the pump mode. Thus we can describe the system further with Bogoliubov theory with changing interaction and find the limits of this description in time.

Therefore we fit the predicted most unstable mode by Bogoliubov theory to the experimental data in the regime $2\pi \times -30 \text{ Hz} < q_{\text{eff}} < 2\pi \times -20 \text{ Hz}$ with nc_1 as a free parameter. From this we calculate the predicted structure size over the whole regime by superposition of the unstable modes as described earlier. In Fig. 21 we see the extracted data for three different evolution times > 60 ms. For 80 ms we find

$$nc_1 = 2\pi \times (14.8 \pm 0.8) \text{ Hz}$$

what is 3 Hz less than the initially determined value. However, the system is over the whole range of measured q_{eff} well described by the predictions made by Bogoliubov theory. For longer evolution time, however, we find differences. Fitting the prediction for 100 ms we find

$$nc_1 = 2\pi \times (12.6 \pm 0.4) \text{ Hz}.$$

For q_{eff} going to zero the structure size is smaller than theoretically predicted while in the regime $q_{\text{eff}} < -nc_1$ the theory fits well. Finally, the system cannot be described over the whole range by Bogoliubov theory with a single nc_1 after 140 ms any more. We can argue that we are out of the regime in that the initial Bogoliubov theory is true. Further, the dynamics differ in speed for different q_{eff} , which prevents a constant nc_1 . We have seen in Fig. 19 that there are additional excitations in the Fourier spectra for times > 120 ms and so the structure size is changed or even dominated by these excitations.

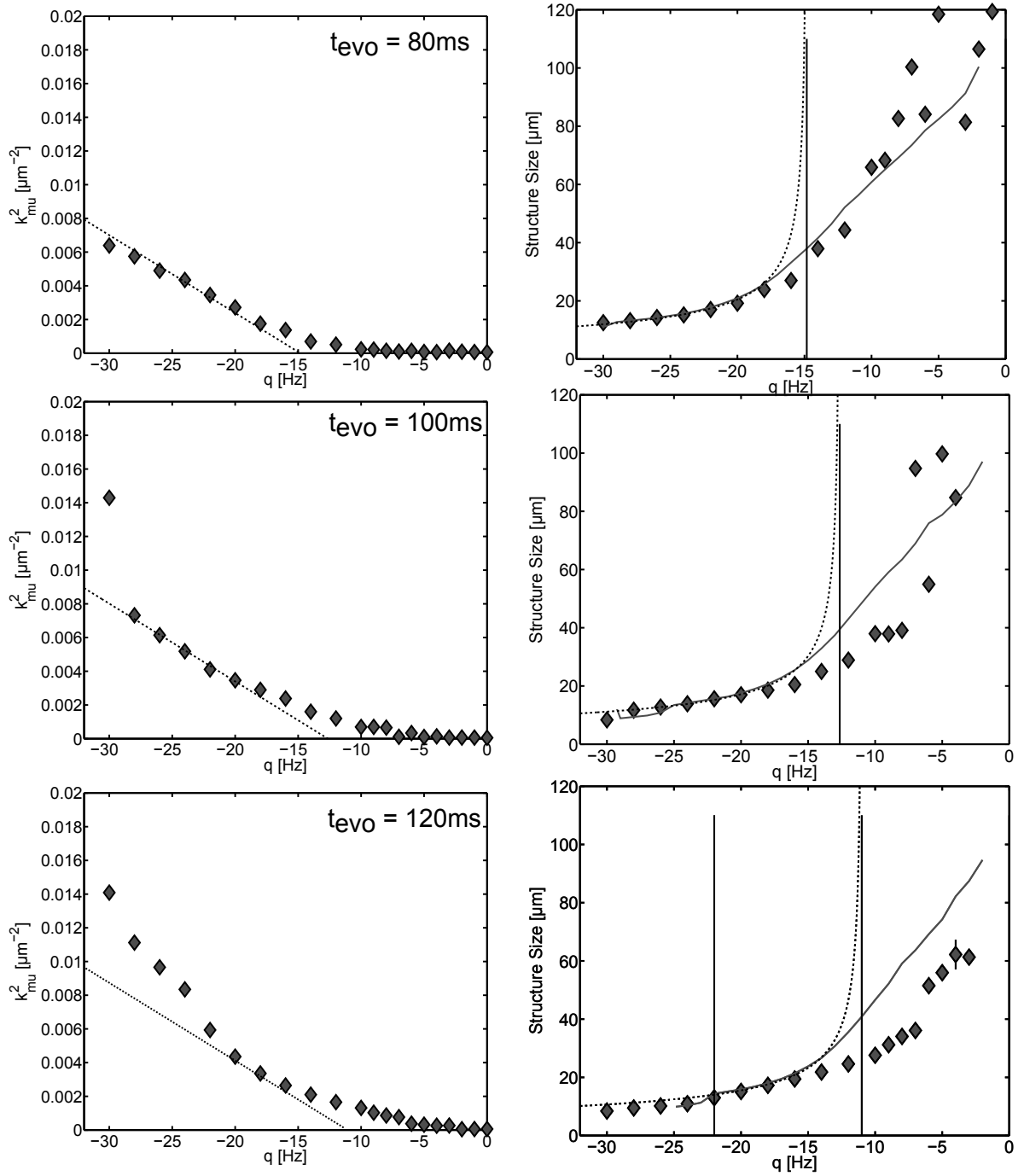


Figure 21: **Comparison of Bogoliubov theory and experimental data with changing interaction strength** Here we show the experimental structure size versus q_{eff} . The data is extracted and plotted as in Fig. 18. For every evolution time the interaction strength nc_1 is fitted. We find $nc_1 = 2\pi \times (14.8 \pm 0.8)$ Hz for 80 ms and $nc_1 = 2\pi \times (12.6 \pm 0.4)$ Hz for 100 ms. For 120 ms we plot the theoretical prediction for comparison with $nc_1 = 2\pi \times 11$ Hz.

6 Conclusion and Outlook

In this thesis, we have presented a comparison of Bogoliubov theory and experimental observation of structure formation in a ^{87}Rb BEC. We showed the controllability of the experimental parameters and the understanding of the short time dynamics.

We drive the system out of equilibrium by quenching the detuning q_{eff} in regimes where the initial state is not stable any more. With this, we tune spin-changing collisions in resonance and occupation numbers in the side modes grow exponentially. Introducing two different methods, the Fourier spectrum of the spin profile and the correlation function, we identified the unstable spatial frequencies and compared them to the prediction made by Bogoliubov theory. We find good agreement for short times up to 60 ms between experiment and theory in the predicted structure sizes. This can be further investigated by comparison to simulations using the truncated Wigner approximation including spatial confinement.

For longer times up to 120 ms the most unstable mode shifts to higher spatial frequencies corresponding to higher energies. This can be explained by an effectively changing interaction strength nc_1 and justified by a comparison of the extracted temporal interaction strength and the time evolution of the linear density. Due to depletion of the pump mode the interaction is dynamically lowered. However, the scaling of the characteristic structure size with q_{eff} can be described by Bogoliubov theory with changed interaction up to ~ 100 ms.

Of future interest is the further time evolution. For non-equilibrium dynamics after quenches interesting quasi steady states as prethermalised states [30] or non-thermal fixed points [31] are predicted. We have already seen in this thesis (Fig. 19) that a second excitation not predicted by Bogoliubov theory appears in the course of the dynamics in the regime of initially stable modes. These could be due to higher order processes, which are triggered by the exponential occupation of the unstable momentum modes [32].

Experimentally it is interesting to investigate how the magnetic field gradient effects the dynamics. Thus, we want to examine the influence by applying different gradients in a controlled fashion. The interaction strength nc_1 is a function of the linear density and variations can lead to changes in the observed structure size. Our spatial confinement leads to inhomogeneous density. Thus, an implementation of a homogeneous potential would give the advantage of a constant interaction nc_1 along the trap.

As mentioned in the beginning, in ^{87}Rb not only $F = 2$ but also $F = 1$ is accessible. As the interaction constant c_1 is negative in this case, we are dealing with ferromagnetic interactions. This leads to a second order phase transition on the boundary of the polar and ferromagnetic ground state [33]. The short time dynamics [34], structure formation [5] and the equilibrium dispersion relation [35] have been extensively studied in a two-dimensional situation. However, for long evolution times scaling in time of the spatial correlation function due to coarsening dynamics is predicted for a two-dimensional situation [36]. It will be interesting to see how the different signs of the interaction affect the long time evolution.

References

- [1] R. P. Feynman, International journal of theoretical physics **21**, 467 (1982).
- [2] A. Lamacraft, Phys. Rev. Lett. **98**, 160404 (2007).
- [3] A. Lamacraft and J. Moore, Ultracold bosonic and fermionic gases **5** (2012).
- [4] D. M. Stamper-Kurn and M. Ueda, Rev. Mod. Phys. **85**, 1191 (2013).
- [5] L. Sadler, J. Higbie, S. Leslie, M. Vengalattore, and D. Stamper-Kurn, Nature **443**, 312 (2006).
- [6] N. Bogoliubov, J.Phys **11** (1947).
- [7] Y. Kawaguchi and M. Ueda, Physics Reports **520**, 253 (2012).
- [8] M. Matuszewski, K. Bongs, and J. Kronjäger, Phys. Rev. A **85**, 023635 (2012).
- [9] J. Kronjäger, C. Becker, P. Soltan-Panahi, K. Bongs, and K. Sengstock, Phys. Rev. Lett. **105**, 090402 (2010).
- [10] T. Zibold, V. Corre, C. Frapolli, A. Invernizzi, J. Dalibard, and F. Gerbier, Phys. Rev. A **93**, 023614 (2016).
- [11] D. A. Steck, *Rubidium 87 D Line Data* (2003).
- [12] H. Pu, C. K. Law, S. Raghavan, J. H. Eberly, and N. P. Bigelow, Phys. Rev. A **60**, 1463 (1999).
- [13] C. Gerry and P. Knight, *Introductory Quantum Optics*(Cambridge University Press) (2005).
- [14] S. Uchino, M. Kobayashi, and M. Ueda, Phys. Rev. A **81**, 063632 (2010).
- [15] L. P. Pitaevskii and S. Stringari, *Bose-einstein condensation*, 116 (Oxford University Press, 2003).
- [16] F. Dalfovo, S. Giorgini, L. P. Pitaevskii, and S. Stringari, Rev. Mod. Phys. **71**, 463 (1999).
- [17] W. Muessel, H. Strobel, M. Joos, E. Nicklas, I. Stroescu, J. Tomkovič, D. B. Hume, and M. K. Oberthaler, Applied Physics B **113**, 69 (2013).
- [18] F. Gerbier, A. Widera, S. Fölling, O. Mandel, and I. Bloch, Phys. Rev. A **73**, 041602 (2006).
- [19] S. Haroche and J. Raimond, “Exploring the quantum: Atoms, cavities and photons, 2006,” .
- [20] M. O. Scully and M. S. Zubairy, *Quantum optics* (Cambridge university press, 1997).

- [21] J. Stenger, S. Inouye, D. Stamper-Kurn, H.-J. Miesner, A. Chikkatur, and W. Ketterle, *Nature* **396**, 345 (1998).
- [22] W. Petrich, M. H. Anderson, J. R. Ensher, and E. A. Cornell, *Phys. Rev. Lett.* **74**, 3352 (1995).
- [23] A. J. Leggett, *Rev. Mod. Phys.* **73**, 307 (2001).
- [24] N. Wiener, *Acta mathematica* **55**, 117 (1930).
- [25] A. Khintchine, *Mathematische Annalen* **109**, 604 (1934).
- [26] E. Nicklas, *A new tool for miscibility control: Linear coupling*, dissertation, University Heidelberg (2012).
- [27] J. D. Sau, S. R. Leslie, D. M. Stamper-Kurn, and M. L. Cohen, *Phys. Rev. A* **80**, 023622 (2009).
- [28] M.-S. Chang, Q. Qin, W. Zhang, L. You, and M. S. Chapman, *Nature Physics* **1**, 111 (2005).
- [29] M. Scherer, B. Lücke, J. Peise, O. Topic, G. Gebreyesus, F. Deuretzbacher, W. Ertmer, L. Santos, C. Klempt, and J. J. Arlt, *Phys. Rev. A* **88**, 053624 (2013).
- [30] J. Berges, S. Borsányi, and C. Wetterich, *Phys. Rev. Lett.* **93**, 142002 (2004).
- [31] B. Nowak, S. Erne, M. Karl, J. Schole, D. Sexty, and T. Gasenzer, arXiv preprint arXiv:1302.1448 (2013).
- [32] J. Berges and J. Serreau, *Phys. Rev. Lett.* **91**, 111601 (2003).
- [33] T.-L. Ho, *Phys. Rev. Lett.* **81**, 742 (1998).
- [34] S. R. Leslie, J. Guzman, M. Vengalattore, J. D. Sau, M. L. Cohen, and D. M. Stamper-Kurn, *Phys. Rev. A* **79**, 043631 (2009).
- [35] G. E. Marti, A. MacRae, R. Olf, S. Lorette, F. Fang, and D. M. Stamper-Kurn, *Phys. Rev. Lett.* **113**, 155302 (2014).
- [36] L. A. Williamson and P. B. Blakie, *Phys. Rev. Lett.* **116**, 025301 (2016).

Danksagung

Zuallererst möchte ich mich bei Markus Oberthaler bedanken, der mir die Möglichkeit gegeben hat das letzte Jahr an diesem spannenden Projekt zu arbeiten und dies auch weiterhin tun zu können. Das vertrauensvolle Arbeitsklima gibt einem die Möglichkeit zielstrebig aber auch gleichzeitig kreativ zu arbeiten.

Thomas Gasenzer danke ich für die Übernahme der Zweitkorrektur und für alles was ich bis jetzt über Bogoliubov Theorie lernen durfte.

Diese Arbeit wäre indes nicht möglich gewesen ohne all meine tollen Kollegen, denen mein großer Dank gilt: Wolfgang hat mich in das Thema eingeführt und mir immer wieder all meine Fragen beantwortet. Dein Abgang ist ein herber Verlust, insbesondere beim Tippspiel zur nächsten EM. Glück auf und Kölle Alaaf! Helmut und Daniel für alle Antworten zu Fragen, die ich gestellt habe und in der Zukunft stellen werde. Danke auch für das Einführen in das Experiment und lange Diskussionen! Philipp, danke für eine tolle Zeit im Labor und wunderbaren Kochabenden mit frischgeschossenem Wild und gutem Wein. Und allen anderen, die Teil des BEC Teams waren, sind und sein werden!

Danke an meinen Politbüro buddy Master Feng für das Einführen von immer mehr sportlichen Aktivitäten! Kollektiv einen großen Dank an den Rest von NAttali! Go, Matterwaver Seeotter, go! AeGis: Grazie, Danke, Merci.

Alle zusammen sorgen für eine wunderbare Arbeitsatmosphäre und schöne gemeinsame Abende an Pizza- und Bäckertagen, sowie außerordentlichen Grillevents.

Unserem Theoretiker Christian danke ich für eine tolle Zeit seit unserer Bachelorarbeit und für unzählige Stunden des Fu- sowie Footballschauens.

Danke an meine Freunde für die schöne Zeit während des Studiums!

Ein großer Dank geht an meine Familie, die mich in allen Lebenslagen immer unterstützt hat. Ich bin froh Teil eines mehrteiligen so toll funktionierenden Familienkomplexes zu sein!

Der größte Dank geht an den wichtigsten Menschen in meinem Leben. Danke für all die gemeinsame Zeit und die Geduld wenn ich mal wieder länger im Büro war.. Ich freue mich auf alles was noch kommen mag!

Erklärung:

Ich versichere, dass ich diese Arbeit selbstständig verfasst habe und keine anderen als die angegebenen Quellen und Hilfsmittel benutzt habe.

Heidelberg, den 28.04.2016

.....